

# Under Pressure: Star Clusters and the Neutral Hydrogen Medium of Tidal Tails

B. Mullan<sup>1</sup>, A. A. Kepley<sup>2,3</sup>, A. Maybhate<sup>4</sup>, J. English<sup>5</sup>, K. Knierman<sup>6</sup>, J. E. Hibbard<sup>3</sup>, N. Bastian<sup>7</sup>, J. C. Charlton<sup>1</sup>, P. R. Durrell<sup>8</sup>, C. Gronwall<sup>1,9</sup>, D. Elmegreen<sup>10</sup>, I. S. Konstantopoulos<sup>11</sup>

## ABSTRACT

Using archival data from ATCA, WSRT, and the VLA, we have analyzed the HI emission of 22 tidal tail regions of the Mullan et al. sample of pairwise interacting galaxies. We have measured the column densities, line-of-sight velocity dispersions, and kinetic energy densities on  $\sim$ kpc scales. We also constructed a tracer of the line-of-sight velocity gradient over  $\sim$ 10 kpc scales. We compared the distributions of these properties between regions that do and do not contain massive star cluster candidates ( $M_V < -8.5$ ;  $\sim 10^4$ – $10^6 M_\odot$  as observed in *HST* WFPC2 VI data). In agreement with Maybhate et al., we find that a local,  $\sim$ kpc-scale column density of  $\log N_{\text{HI}} \gtrsim 20.6 \text{ cm}^{-2}$  is frequently required for detecting clustered star formation. This HI gas also tends to be turbulent, with line-of-sight velocity dispersions  $\sigma_{\text{los}} \approx 10$ – $75 \text{ km s}^{-1}$ , implying high kinetic energy densities ( $\log \Sigma_{\text{KE}} > 46 \text{ erg pc}^{-2}$ ). Thus high HI densities and pressures, partly determined by the tail dynamical age and other interaction characteristics, are connected to large-scale cluster formation in tidal tails overall. Lastly, we find that the high mechanical energy densities of the gas are likely not generally due to feedback from star formation. Rather, these properties are more likely to be a cause of star formation than a result.

*Subject headings:* galaxies: ISM, galaxies: interactions, galaxies: star clusters, radio lines: galaxies

<sup>1</sup>Pennsylvania State University, Department of Astronomy & Astrophysics, 525 Davey Lab University Park PA 16803; mullan@astro.psu.edu

<sup>2</sup>Department of Astronomy, University of Virginia, P.O. Box 400325, Charlottesville, VA 22904-4325

<sup>3</sup>National Radio Astronomy Observatory, 520 Edgemont Road, Charlottesville, VA 22903-2475

<sup>4</sup>Space Telescope Science Institute, 3700 San Martin Drive, Baltimore, MD 21218

<sup>5</sup>University of Manitoba, Department of Physics and Astronomy, Winnipeg, Manitoba R3T 2N2, Canada

<sup>6</sup>Arizona State University, School of Earth and Space Exploration, Bateman Physical Sciences Center F-wing Room 686, Tempe, AZ 85287-1404

<sup>7</sup>Excellence Cluster Universe, Technische Universität München, Boltzmannstraße 2, Garching, Germany

<sup>8</sup>Youngstown State University, Department of Physics and Astronomy, Youngstown, OH 44555

<sup>9</sup>Institute for Gravitation and the Cosmos, The Pennsylvania State University, University Park, PA 16802

<sup>10</sup>Vassar College, Department of Physics & Astronomy, Box 745, Poughkeepsie, NY 12604

<sup>11</sup>Australian Astronomical Observatory, PO Box 915, North Ryde NSW 1670, Australia

## 1. Introduction

Tidal tails are common products of disk galaxy interactions (e.g., Toomre 1977; Schweizer 1978). These extended, pronounced structures begin their lives shortly after the initial encounter of their progenitor galaxies, drawn from a combination of ISM and stars of these systems' outer regions. While relatively short-lived ( $\lesssim 1$  Gyr), tidal debris exhibits an extraordinary variety of morphological and kinematic phenomena. These range from long, thin tails, to diffuse plumes, to kinematically distinct tidal dwarf galaxies (TDGs), all characteristic of the numerous interactions that populate the Local Volume (Duc et al. 2004).

Tidal tails are composed of  $\sim 10^9 M_\odot$  of gas—and some small underlying population of stars—pulled from the outer regions of their host galaxies by gravitational torques and the tidal

field induced by an encounter with another system (see Bournaud 2011 for a review). Although there are wide variations in metallicity by galaxy, studies of non-interacting disk galaxies indicate that gas from these regions prior to the interaction are generally HI-rich and metal/H<sub>2</sub>-poor (Bigiel et al. 2010). The neutral hydrogen medium is thus the *de facto* tracer of the kpc-scale ISM in tidal tails, and has a long history of observation (e.g., van der Hulst 1979; Simkin et al. 1987; Appleton et al. 1987; Yun et al. 1994; Horellou & Koribalski 2007; Sengupta et al. 2012). Decades of study have revealed that the HI in tidal debris is a generally inhomogeneous, kinematically disturbed medium, subject to a variable tidal potential throughout the course of the interaction that can be both locally “extensive” (pulling material apart) and “compressive” (pushing it together; Renaud et al. 2009).

The importance of HI column density,  $N_{\text{HI}}$ , in star formation has observational precedent in many extragalactic environments. In a self-gravitating gas disk, stability analysis shows there is likely a threshold  $N_{\text{HI}}$  that permits it (Kennicutt 1989). This may be true across a variety of cosmic venues. On  $\sim 500$  pc<sup>2</sup> scales within dwarf irregular galaxies, this threshold may be  $\approx 10^{21}$  cm<sup>-2</sup> (Skillman & Bothun 1986; Skillman 1987). Moreover, UV emission—a key diagnostic for recent star formation in the past  $\sim 100$  Myr—is observed where the HI column density reaches or exceeds  $\approx 2.5 \times 10^{20}$  cm<sup>-2</sup> (Neff et al. 2005; Thilker et al. 2005; Gil de Paz et al. 2005). This is consistent with Schaye (2004), who determine that a minimum surface density of  $\approx 3 M_{\odot}$  pc<sup>-2</sup> is necessary to first form a cold neutral phase, with some dispersion from metallicity and the interstellar radiation field. The production of the cold molecular hydrogen necessary for gravitational collapse and star formation would then occur, the amount of which is controlled largely by the HI density (Krumholz et al. 2009). The ratio of H<sub>2</sub> to HI surface densities increases almost linearly with interstellar pressure and the HI densities that promote it, and saturates at a mass density of  $\sim 10 M_{\odot}$  pc<sup>-2</sup> (Wong & Blitz 2002; Blitz & Rosolowsky 2004; Blitz & Rosolowsky 2006; Walter et al. 2008; Leroy et al. 2008). Star formation may then scale with respect to the density and amount

of molecular gas available for collapse (e.g., Kennicutt 1998; Liu et al. 2011 and references therein).

In tidal tails, large distances ( $\lesssim 100$  Mpc) and low surface brightnesses can make observing this star formation difficult. Compact star clusters and their populations are therefore convenient surrogates for this task; they can be considered high-signal, luminous tracers of the local star formation history of their environments (Konstantopoulos 2010; de Grijs 2010). The most massive ( $\sim 10^5$ – $10^6 M_{\odot}$ ) of these star clusters or cluster candidates have been observed in some tidal tails (de Grijs et al. 2002; Tran et al. 2003; Bastian et al. 2005), but not all (Mullan et al. 2011; Knierman et al. 2003). This implies that the conditions required for extensive star cluster formation (and the detection of the most massive clusters by the size-of-sample effect; e.g., Gieles & Bastian 2008) are not always present in these environments. Consequently, tails may occupy the edge of the physical parameter space that allows these structures to form and/or survive.

The content and character of the observable HI medium may have a role to play in star cluster formation. Maybhate et al. (2007) examined a sample of tidal debris from late-stage ( $\gtrsim 400$  Myr old) interactions and determined that a local,  $\sim$ kpc-scale HI column density of  $\approx 10^{20.6}$  cm<sup>-2</sup> or higher is required for finding significant populations of luminous star clusters. This is similar to the results of Walter et al. (2006), who find that HII regions are only observed where  $\log N_{\text{HI}} \geq 21.0$  cm<sup>-2</sup> on 200-pc<sup>2</sup> scales for the tidal arms of NGC 3077.

However, Maybhate et al. (2007) stipulate that  $N_{\text{HI}}$  is not a sufficient condition for finding bright, massive star clusters. They cite the debris of NGC 3921 as an environment where a non-negligible fraction of neutral hydrogen exists above their fiducial threshold value, but massive star clusters are unlikely to exist. Other properties related to the kinematics of the HI medium may also be important. For instance, disruptive shear might influence a star-forming environment to “prefer” forming associations over bound clusters (Weidner et al. 2010). This may be observed in the central regions of the Antennae, where Whitmore et al. (1999) do not find massive clusters where the line-of-sight velocity gradient is high.

Morphological asymmetries in the optical and HI debris components also indicate that other, large-scale physics may influence the HI-star cluster connection. Dust obscuration, ram-pressure stripping by the galaxy interaction, and photoionization from a central galactic superwind or locally by a previous generation of efficient star formation (Hibbard et al. 2000) may additionally confuse the issue. Some of these phenomena, along with the bulk properties of the tidal tail, will be dependent on age, initial galactic orientations and speeds, and other properties of the interactions themselves (Duc et al. 2004).

The inconsistent production of star cluster populations in tidal tails may also be partially due to the kinematic character of the  $\sim$ kpc-scale HI medium. Under “normal” circumstances in many parts of isolated galaxies, the HI medium generally consists of a mixture of cold ( $T \sim 100$  K) HI clouds embedded in a warm HI medium ( $T \sim 8000$  K) with characteristic thermal linewidths  $\approx 6\text{--}8$  km  $s^{-1}$  (McKee & Ostriker 1977; Wolfire et al. 1995; Wolfire et al. 2003). Past the canonical optical boundary  $R_{25}$ , the warm ISM may be heated by UV radiation from the interior galaxy or the extragalactic background (Schaye 2004). In tidal tails, however, observed linewidths often exceed thermal values. These motions are typically attributed to turbulence in the gas, which may be generated by feedback from star formation (Tamburro et al. 2009) or magnetic effects (e.g., Sellwood & Balbus 1999). Perhaps most importantly, turbulence can also be produced by the large-scale shocks and gravitational instabilities triggered by the interaction (Bournaud 2010).

The *pressures* exerted by turbulent warm HI and the reservoir of high-density gas they produce may therefore engender the conditions necessary for pockets of the cold neutral medium (Wolfire et al. 2003) to exist on unobservable  $\sim$ pc scales. If provided ample dust, these regions become sites for  $H_2$  production and subsequent star formation. Observationally, interacting systems do indeed appear to generally contain more molecular gas than their quiescent counterparts (Casasola et al. 2004). If gas becomes too turbulent, however, it may interfere with its own cooling processes (Wolfire et al. 2003) and prevent high-density molecular gas from either forming, or cooling efficiently if already present. For ex-

ample, Guillard et al. (2012) detect highly turbulent CO (with velocity dispersions  $\gtrsim 100$  km  $s^{-1}$ ) in collisionally shocked regions of Stephan’s Quintet. These regions also have low PAH-to-CO surface luminosities, indicating low star formation efficiency from an evidently high gas heating rate. Moreover, sufficient HI density must be required to build enough  $H_2$  to self-shield from photodissociation by the extragalactic background or relatively nearby stellar sources. Thus, it is likely that star formation is contingent on HI density as well as kinematics, dictated by large ( $\sim$ kpc)-scale phenomena.

Interstellar pressure not only enhances star formation in general, but it may also help dictate the types of stellar “packaging” that are produced. In tidal tails, the presence of dense, turbulent gas may conceivably encourage the formation of tidal dwarf galaxies (Elmegreen 1993; Elmegreen & Efremov 1997) or other bound structures like compact star clusters. High pressures help prevent a cluster from disruption in its early gas expulsion phase (e.g., Whitmore, Chandar, & Fall 2007; Bastian & Gieles 2008; and references therein). If star formation depends on gas density, then high pressures promote clustered star formation at a rate that increases as the local star formation rate (SFR) increases (Larsen & Richtler 2000). In addition, Elmegreen (2008) finds that bound clusters can form at lower average densities at high Mach numbers than at low Mach numbers; thus the threshold density needed to form clusters is effectively reduced in highly turbulent media and clusters can become a favored “mode” of star formation.

Tidal tails appear to offer a unique environment where the individual HI-related variables that may influence star cluster formation can be systematically tested. In this paper, we explore the complex relationship between galaxy interactions, their effects on the HI medium in their tidal tails, and the star clusters that are selectively found within. This study is the first detailed investigation of the kpc-scale column densities and kinematic character of the neutral hydrogen medium and its relationship to star cluster populations in this type of extragalactic environment. We extend the sample of merging galaxies of Maybhatte et al. (2007) and Knierman et al. (2003) with archival Very Large

Array (VLA), Australia Telescope Compact Array (ATCA), and Westerbork Synthesis Radio Telescope (WSRT) 21-cm observations of the tidal tail sample studied by Mullan et al. (2011). The 22 tails total span a wide range of dynamical ages, merging mass ratios, and previously established star cluster population sizes and characteristics. An overview of the HI observations and reduction is provided in Section 2, along with selection of star cluster candidate positions and photometry from optical data. In Section 3, we present our methods of measuring various HI quantities, e.g., column density and velocity dispersion. We examine the local HI characteristics of the tails with respect to the cluster populations in Section 4. We present our results in Section 5, and discuss trends and differences in the HI content among established types of interactions. In this section we also examine turbulence and its role as a cause or result of star formation. Lastly, we offer conclusions and final remarks in Section 6.

## 2. Observations

### 2.1. The Tidal Tail Sample and Their Star Cluster Candidates

We obtained the *HST* WFPC2 data for the tidal tail regions studied by Mullan et al. (2011); hereafter M11, Maybhate et al. (2007), and Knierman et al. (2003). These include contributions from cycles 7 (GO-7466) and 16 (GO-11134), with imaging performed in the F555W/F814W and F606W/F814W bands, respectively. The systems that produced these tails were originally selected to represent a large parameter space of observable and dynamical characteristics of galaxy interactions present in the local universe, from optical/HI properties, to progenitor mass ratios, to interaction ages (M11). In this study, we use the same naming convention for debris regions as these publications; e.g., NGC 1487E and NGC 1487W refers to the eastern and western tails of NGC 1487, respectively, while the three WFPC2 pointings of NGC 4038/9 are denoted by NGC 4038A, NGC 4038B, and NGC 4038C.

We also acquired the source catalogs of J2000 positions and photometry of compact objects detected in Maybhate et al. (2007) and M11; the latter contains sources detected by Knierman et al.

(2003). Source photometry had been transformed from F555W/F606W and F814W to standard  $V$  and  $I$  bandpasses with the Holtzman et al. (1995) prescription<sup>1</sup> in these studies to facilitate comparison with the earlier photometry published in standard magnitudes. Photometry had also been corrected for Galactic extinction using Schlegel, Finkbeiner, & Davis (1998) and Girardi et al. (2008); see M11 and Knierman et al. (2003) for details. Objects detected and measured with this methodology were defined as star cluster candidates (SCCs) if they met the following color-magnitude criteria:

- $M_V < -8.5$ . Many studies use a similar magnitude cutoff ( $M_V = -8$  to  $-9$ : Knierman et al. 2003; Knierman 2007; Schweizer et al. 1996; Whitmore et al. 1999) because of detection limits and the threat of contamination from non-cluster sources at fainter magnitudes. Source detection within the tail regions of the M11 sample was previously found to be more than 50% complete at  $M_V < -8.5$ , so we implement this criterion here. M11 also reaffirmed the findings of Efremov & Ivanov (1987); i.e. that this magnitude limit sufficiently protects against contamination from single main sequence and post main sequence stars.
- $V - I < 1.0$ . This allows for a wide range of possible metallicities, extinctions, and ages in our cluster population (e.g., Peterson 1993; Ajhar, Blakeslee, & Tonry 1994, Whitmore et al. 1995; Kundu & Whitmore 2001). This  $V - I$  limit was also selected to reflect uncertainties or additional reddening from dynamical (Portegies Zwart et al. 2010), stochastic (Maíz Apellániz 2009), and disruptive (Anders et al. 2009) effects.

For similar reasons, M11 and Maybhate et al. (2007) used  $V - I < 2.0$  as a color limit in their work. In practice, comparing the completeness curves of in-tail vs. out-of-tail areas reveal relatively limited tail extinctions ( $A_V \sim 0.5$ ; M11), and stochastic effects should be restricted to  $V - I$

<sup>1</sup>M11 employed updated methods for recent data and instrumental characteristics documented in [http://purcell.as.arizona.edu/wfpc2\\_calib/2008\\_07\\_19.html](http://purcell.as.arizona.edu/wfpc2_calib/2008_07_19.html).

changes at the  $\lesssim 5\%$  level (Anders et al. 2009) for the  $M_V < -8.5$ ,  $\sim 10^5$ – $10^6 M_\odot$  clusters we study. Furthermore, an examination of the M11 sources and their color-magnitude diagrams reveals that a more stringent cutoff helps reduce the number of out-of-tail and presumably background sources detected, which tend to be redder ( $V - I \gtrsim 1$ ). These results are substantiated by the multiwavelength observations and selection criteria of Trancho et al. (2012).

## 2.2. HI Calibration and Reduction

Table 1 lists the tails from M11, Knierman et al. (2003), and Maybhate et al. (2007) for which archival HI data exist (22 tails total). We include the dynamical ages and mass ratios of these interacting systems for later reference. Our mass ratio values and tail ages are taken directly from M11 and sources therein. The mass ratio is defined as  $M_1/M_2$ , where  $M_1$  and  $M_2$  are the respective masses of the perturbing and main galaxies. Upon further review, we inverted the reported mass ratios of NGC 2782E and NGC 4747 (to 4 and 20) to reflect the understanding in the literature that the tail regions examined here are likely pulled from the smaller-massed galaxies of their interactions.

Neutral hydrogen data for NGC 1614, NGC 2782, NGC 2992/3, NGC 2444, and NGC 2535 were taken from the VLA archives<sup>2</sup>. The data were reduced in AIPS using the standard procedures detailed in the AIPS Cookbook<sup>3</sup>. Here we provide a brief outline of this methodology. In addition to the program source, a bright primary (gain) calibrator and a secondary (phase) calibrator were observed. The primary calibrator was usually observed at least once in the observing program and the secondary calibrator observed every approximately 40 minutes to an hour of time on source. Using the channel-0 data, the flux density of the primary calibrator was found using *setjy*. Then the amplitudes and phases of both the primary calibrator and the secondary calibrator were determined using *calib*. The flux density of the secondary calibrator was

determined from the primary calibrator using the task *getjy*. The calibration was applied to the source using *lcal*. The channel-zero calibration solutions were copied to the spectral line data. Finally, the spectral line data was bandpass calibrated in *bpass* using the primary calibrator.

The calibrated data were test imaged in *imagr* and the line-free channels determined. Using this information, the data were continuum subtracted using *uvlsf*. The final, continuum subtracted images were produced in *imagr*; the data were imaged with varying values of the “robust” weighting parameter (Briggs et al. 1999), with values from 0–5. A larger robust parameter enhances detection of diffuse HI emission at the expense of angular resolution. In most cases, the diffuse emission was resolved out of the high resolution image. In the case of two overlapping intermediate frequencies (IFs), the images in the overlapping channels were averaged and a combined cube formed.

We acquired a reduced data cube for NGC 4747 from the Westerbork Synthesis Radio Telescope (WSRT) web archive<sup>4</sup>. These data were originally taken, calibrated, and reduced as a part of the WHISP program (van der Hulst et al. 2001). Here, we use the cube generated to  $\approx 60''$  resolution, which we found was an appropriate balance between spatial resolution and detecting low-signal HI in the tidal regions of NGC 4747.

The neutral hydrogen data for NGC 6872 and NGC 1487 were obtained from the ATCA archives. The NGC 1487 data were processed using Miriad (Sault et al. 1995) for all steps, including the calibration (with the tasks *wvflag*, *blflag*, and *mfcal*) and removal of continuum (with the task *uvlin*). The primary calibrators were 1934-638 and 1151-348, while the secondary was 0332-403. We produced images by combining the array configurations listed in Table 1—using standard tasks *invert*, *clean*, and *restor*. The data for NGC 6872 were calibrated with a combination of AIPS and Miriad. AIPS was used to flag (*spflag*) and image the data (*imagr*), while data was calibrated (using *mfcal* because the nearby primary calibrator 1934-638 was used as the secondary calibrator) in Miriad. The ATCA does not doppler track, so

<sup>2</sup>The National Radio Astronomy Observatory is a facility of the National Science Foundation operated under cooperative agreement by Associated Universities, Inc

<sup>3</sup><http://www.aips.nrao.edu/cook.html>

<sup>4</sup>The Westerbork Synthesis Radio Telescope is operated by the Netherlands Institute for Radio Astronomy ASTRON, with support of NWO.

the correct velocity definition was determined in Miriad and applied to the data in AIPS using the task *cvel*.

We also obtained the reduced cubes used by Maybhate et al. (2007) in their HI analysis. Their reduction strategies are similar, optimizing diffuse HI emission in the VLA-observed tails of NGC 4038, NGC 7252, and NGC 3921, and the ATCA-observed tails of NGC 3256. Data for NGC 520 were obtained from Hibbard & van Gorkom (1996). A brief description of all radio data is presented in Table 1. Table 1 includes source distances, beam dimensions ( $b_1$  and  $b_2$ ), and beam position angles (P.A.). We also list angular and physical pixel areas ( $A_{\text{pix}}$ ), channel widths ( $dv$ ),  $1\sigma$  detection limits in single channel integrated flux densities  $\epsilon_{S_i} dv$  ( $10^{-4}$  Jy km s $^{-1}$  channel $^{-1}$ ) and column densities  $\epsilon_{N_{\text{HI}}}$  array setups, and original publications and/or project codes for the observations. We use luminosity distances for all systems (assuming  $H_0 = 73$  km s $^{-1}$  kpc $^{-1}$ ), except for NGC 4038 where we adopt the distance measurement of Saviane, Hibbard, & Rich (2004). This was done for consistency with M11. All cubes were pre-processed to J2000 for direct comparison with SCC positions.

A cursory glance at Table 1 shows that the pixel sizes of the cubes are not a fixed fraction of the beam sizes. The size and dimensions of the synthesized beam depend on the sampling (and weighting/tapering) of the  $uv$  plane in observing these sources, which is a function of the array configurations used, observation program design, and source declination. Works cited in the Original Publications column contain additional information on these issues for each observation. The pixel size, meanwhile, is chosen to avoid undersampling the beam (fewer than  $\approx 2$ – $3$  pixels across the beam) and avoid large computational times ( $\gtrsim 10$  pixels across the beam, depending on the original map size). Different pixel sizes are selected between these extremes to maintain sufficient signal within pixels and individual channels for the varying source intensities of the tidal tail sample.

### 3. Analysis

Our reduced and calibrated cubes contain three dimensions: the typical x/y astrometric compo-

nents, and frequency. Each element of the cube registers the intensity (Jy beam $^{-1}$ ) at a certain position and over a particular channel of observed frequency, which tracks the HI emission over velocity space. These elements and their errors can be transformed into measurements of flux density (Jy) by multiplying the intensity by the ratio of the pixel and beam angular sizes,  $A_{\text{pix}} A_{\text{beam}}^{-1}$ , whose values are recorded in Table 1.

Our immediate objective is to probe the HI properties on the smallest physical scales afforded by our data cubes, specifically where there are established cluster candidates. Maybhate et al. (2007) produced maps of the HI column density for their sample of tidal tails and determined the underlying  $N_{\text{HI}}$  values for each of their SCC positions. Given the differences in resolution scales between their optical and radio data, this was in essence a pc-to-kpc comparison. Here, we instead identify areas in our HI data that “contain” SCCs and compare those to the areas that do not. This is a favorable kpc-to-kpc spatial comparison.

We are therefore concerned with the spectrum of HI emission of different xy positions within the smallest regions possible. Individually the resolution of each cube is set by the synthesized beam ( $\sim$  several kpc in this sample), which for the purposes of interferometric imaging is sampled by the selected pixel size ( $\sim 0.1$ – $2$  kpc). In the sections below we map out HI characteristics from the cubes on a pixel-by-pixel basis. Because this project is a synthesis of optical and radio data and terminology, we will continue to use the term “pixel” to describe the xy components of our data cubes. Each pixel thus contains a one-dimensional cross section of the cube corresponding to all frequency (velocity) channels of an individual spatial position. Extracting and characterizing these spectra for every pixel with sufficient HI signal in an established tail region is our critical task, requiring careful pixel and channel selection. Not all channels of a given pixel will contain HI signal, which necessitates careful masking of “noise” channels and selection of “signal channels” to properly ascertain HI properties for that pixel. We describe our technique, implemented with the Interactive Data Language (IDL), below.

**Table 1.**  
Tidal Tail Observations

Tail	Dist. <sup>a</sup> (Mpc)	Age <sup>b</sup> (Myr)	Mass Ratio <sup>c</sup>	b <sub>1</sub> <sup>d</sup>	b <sub>2</sub> <sup>d</sup>	Beam P.A. <sup>e</sup>	A <sub>pix</sub> <sup>f</sup> (arcsec <sup>2</sup> )	A <sub>pix</sub> <sup>g</sup> (kpc <sup>2</sup> )	dv <sup>h</sup>	ε <sub>S<sub>i</sub></sub> dv <sup>i</sup>	log ε <sub>N<sub>H<sub>I</sub></sub><sup>j</sup></sub>	Project Codes <sup>l</sup>
Instruments and Arrays <sup>k</sup>								Original Publications				
The Mullan et al. (2011) Sample												
NGC 1487E	10.8	500	0.25	27.0	24.1	16.1	9	0.02	10	0.93	19.11	C531
				ATCA 375 + 750A + 1.5A + 1.5B + 1.5D + 6A					Getts (2001); English & Freeman (2001)			
NGC 1487W	10.8	500	0.25	27.0	24.1	16.1	9	0.02	10	0.93	19.11	C531
				ATCA 375 + 750A + 1.5A + 1.5B + 1.5D + 6A					Getts (2001); English & Freeman (2001)			
NGC 4747	20.2	320	20	61.9	48.5	0.00	400	3.84	16.4	39.47	19.09	-
				WSRT					van der Hulst et al. (2001)			
NGC 520	27.2	300	0.05	24.5	23.8	38.3	25	0.43	10.5	1.13	18.75	AH412/ AH417
				VLA C + D					Hibbard & van Gorkom (1996)			
NGC 2992	36.6	100	1	23.9	17.9	-14.9	16	0.50	20.5	2.78	19.34	AD402
				VLA C					Duc et al. (2000)			
NGC 2993	36.6	100	1	23.9	17.9	-14.9	16	0.50	20.5	2.78	19.34	AD402
				VLA C					Duc et al. (2000)			
NGC 2782E	38.1	200	4	19.8	17.9	86.4	4	0.14	10.3	0.53	19.22	AS389/ AS453
				VLA B + C + D					Smith (1997); Smith (1994); Smith (1991)			
NGC 2782W	38.1	200	0.25	19.8	17.9	86.4	4	0.14	10.3	0.53	19.22	AS389/ AS453
				VLA B + C + D					Smith (1997); Smith (1994); Smith (1991)			
NGC 2444	58.2	100	0.50	27.9	27.1	-34.2	16	1.28	20.5	1.70	19.12	AA63
				VLA C + D					Appleton et al. (1987)			
NGC 2535	59.8	100	0.30	20.4	18.4	16.6	9	0.76	5.1	0.87	19.08	AK327
				VLA C + D					Kaufman et al. (1997)			
NGC 6872E	62.6	150	0.20	53.5	51.6	25.1	16	1.46	19.8	1.64	19.11	C979
				ATCA 750D + EW352 + 1.5G + 750F					Horellou & Koribalski (2007)			
NGC 6872W	62.6	150	0.20	53.5	51.6	25.1	16	1.46	19.8	1.64	19.11	C979
				ATCA 750D + EW352 + 1.5G + 750F					Horellou & Koribalski (2007)			

Continued on next page...

Table 1. Continued

Tail	Dist. <sup>a</sup> (Mpc)	Age <sup>b</sup> (Myr)	Mass Ratio <sup>c</sup>	b <sub>1</sub> <sup>d</sup>	b <sub>2</sub> <sup>d</sup>	Beam P.A. <sup>e</sup>	A <sub>pix</sub> <sup>f</sup> (arcsec <sup>2</sup> )	A <sub>pix</sub> <sup>g</sup> (kpc <sup>2</sup> )	dv <sup>h</sup>	ε <sub>S<sub>i</sub></sub> dv <sup>i</sup>	log ε <sub>N<sub>HI</sub></sub> <sup>j</sup>	Project Codes <sup>l</sup>
Instruments and Arrays <sup>k</sup>									Original Publications			
The Mullan et al. (2011) Sample												
NGC 1614N	65.6	750	1	15.0	10.0	-83.0	9	0.91	10.6	3.09	19.63	AH0527
				VLA C + D					Hibbard & Yun (1996)			
NGC 1614S	65.6	750	1	15.0	10.0	-83.0	9	0.91	10.6	3.09	19.63	AH0527
				VLA C + D					Hibbard & Yun (1996)			
The Knierman et al. (2003)/Maybhatte et al. (2007) Sample												
NGC 4038A	13.8	420	1	20.7	15.4	24.3	25	0.11	5.2	3.17	19.20	AG0516
				VLA C + D					Hibbard et al. (2001)			
NGC 4038B	13.8	420	1	20.7	15.4	24.3	25	0.11	5.2	3.17	19.20	AG0516
				VLA C + D					Hibbard et al. (2001)			
NGC 4038C	13.8	420	1	20.7	15.4	24.3	25	0.11	5.2	3.17	19.20	AG0516
				VLA C + D					Hibbard et al. (2001)			
NGC 3256E	42.8	400	1	25.7	19.3	6.94	16	0.69	33.5	13.06	20.01	C061
				ATCA 1.5B + 1.5C + 1.5D					English et al. (2003)			
NGC 3256W	42.8	400	1	25.7	19.3	6.94	16	0.69	33.5	13.06	20.01	C061
				ATCA 1.5B + 1.5C + 1.5D					English et al. (2003)			
NGC 7252E	62.2	730	1	26.9	16.1	18.6	25	2.28	42.5	4.53	19.35	AH0372/ AH0412
				VLA C + D					Hibbard et al. (1994)			
NGC 7252W	62.2	730	1	26.9	16.1	18.6	25	2.28	42.5	4.53	19.35	AH0372/ AH0412
				VLA C + D					Hibbard et al. (1994)			
NGC 3921S	84.5	460	1	19.3	18.1	-85.1	25	4.20	10.7	1.61	18.91	AH0417
				VLA C + D					Hibbard & van Gorkom (1996)			

**Notes.**

<sup>a</sup>Luminosity distance (Mpc)

<sup>b</sup>Dynamical age from M11 and sources therein (Myr)

<sup>c</sup>Defined as  $M_1/M_2$ , with  $M_1$  and  $M_2$  the mass of the progenitor and perturbing galaxy, respectively

<sup>d</sup>Beam dimensions (arcsec)

<sup>e</sup>Beam position angle (deg)

<sup>f</sup>Single pixel area (arcsec<sup>2</sup>)

<sup>g</sup>Single pixel area (kpc<sup>2</sup>)

<sup>h</sup>Channel width (km s<sup>-1</sup>)

<sup>i</sup>1σ detection limit in the single channel integrated flux density (10<sup>-4</sup> Jy km s<sup>-1</sup> channel<sup>-1</sup>)

<sup>j</sup>1σ detection limit in column density (cm<sup>-2</sup> channel<sup>-1</sup>)

<sup>k</sup>Instruments (ATCA, WSRT, or VLA) and array configurations used in original data acquisition (see original publications for details)

<sup>l</sup>ATCA and VLA archive project and proposal codes of acquired data



### 3.1. Channel Selection

We first apply channel selection criteria to all pixels, to identify the channels in which HI emission is confidently identified. There are a variety of methods to identify signal in individual channels of an HI pixel and to mask channels without. For instance, THINGS (The HI Nearby Galaxy Survey; Walter et al. 2008) required that a signal be registered by at least three contiguous channels (each of a width  $\lesssim 5 \text{ km s}^{-1}$ ). Their instrument setup was designed to Nyquist sample the warm neutral medium, and they report that this method sufficiently highlights real 21-cm emission and eliminates noise.

Our data exhibit a much wider range of channel widths, from  $\approx 5.13$  to  $42.5 \text{ km s}^{-1}$ , so we must avoid such a constraint for cubes where multiple channels would span an unrealistically broad velocity space. Moreover, our data are inhomogeneous in sensitivity, so the appearance of an HI line profile may vary depending on these instrumental constraints and orientation/projection effects. Thus, we customized the channel selection criteria for each tail after examining the spectra of many pixels across the tidal debris. Table 2 lists the channel selection requirement as a signal-to-noise ratio for single channel signal and equivalent integrated flux density for each tail, along with the minimum number of adjacent channels  $N_{\text{chan}}$  needed at that flux density for a pixel to count as signal.

The values in Table 2 were selected after an extensive trial-and-error process for each tail that produced reasonable spectra and maps of the properties described in Section 3.3 below. We varied both  $N_{\text{chan}}$  and the necessary signal-to-noise ratio until no single, isolated pixels in maps of the line-of-sight velocity dispersion ( $\sigma_{\text{los}}$ ) registered physically unrealistic values within the tail regions (i.e.  $\gtrsim 150 \text{ km s}^{-1}$ , depending on the tail). Pixels within a beam size are statistically correlated, so finding occasional pixels with discrepant values in velocity dispersion maps indicated that noisy channels outside the velocity space of actual emission were unwittingly selected and thus tended to increase  $\sigma_{\text{los}}$  relative to the surrounding pixels. The spectra of these locations were also visually studied to optimize our masking parameters.

**Table 2.**  
Single Channel Signal Detection Criteria

Tail	S/N <sup>a</sup>	$S_{\text{min}}dv^b$	$N_{\text{chan}}^c$
NGC 1487E	2.75	2.56	2
NGC 1487W	2.75	2.56	2
NGC 4747	3.00	118.42	1
NGC 520	2.25	2.55	3
NGC 2992	2.50	6.95	2
NGC 2993	2.50	6.95	2
NGC 2782E	2.25	1.20	2
NGC 2782W	2.25	1.20	2
NGC 2444	2.00	3.40	2
NGC 2535	2.25	1.96	3
NGC 6872E	2.25	3.70	2
NGC 6872W	2.25	3.70	2
NGC 1614N	2.25	6.95	2
NGC 1614S	2.25	6.95	2
NGC 4038A	2.25	7.14	3
NGC 4038B	2.75	8.73	2
NGC 4038C	2.75	8.73	2
NGC 3256E	3.50	45.70	1
NGC 3256W	3.50	45.70	1
NGC 7252E	3.50	15.86	1
NGC 7252W	3.50	15.86	1
NGC 3921S	2.00	3.23	3

**Notes.**

<sup>a</sup>Signal-to-noise ratio required for a single channel

<sup>b</sup>Minimum integrated flux density required for a single channel ( $10^{-4} \text{ Jy km s}^{-1}$ )

<sup>c</sup>The number of adjacent channels needed at the indicated flux to register HI emission in a pixel

We then masked out, i.e. ignored, the noise channels in the cube, with the exception of noise channels alongside channels containing signal. These were left unmasked, as were all adjacent channels until a flux density level consistent with  $0 \text{ Jy}$  ( $\pm 1\sigma$ ) was found along either side of those original signal channels. This helped to prevent clipping of broad spectral features present across multiple channels. If any of these additional channels registered flux densities below  $0 \text{ Jy}$ , they were then masked to discourage biasing any measurements toward lower values. When integrated, the unmasked pixels provide a total signal typically  $>3\sigma$  over the channel-integrated r.m.s. noise.

We display several examples of results from our signal selection procedure in Figure 1 and

Figure 2. A spectrum from one randomly selected pixel from each tail is shown in these figures, plotted in gray; the overplotted error bars indicate the r.m.s. noise. Signal channels are indicated as black points. The heterogenous channel widths and noisy quality of some of the randomly chosen HI profiles are clearly evident in these figures, highlighting the need for a varied signal selection criteria across the sample.

### 3.2. Pixel Selection

We also limit our analysis to regions in our HI data encompassed by previous optical observations, i.e., selecting HI pixels that are “in-tail” and within the WFPC2 FOV of the previous studies. Within the WFPC2 images of their datasets, M11 and Knierman et al. (2003) defined areas that were at least one count above the sky level in F606W or F555W as “in-tail.” These groups used the WF2–4 chips in their analysis, choosing to ignore the planetary camera with its prohibitively high readnoise. Maybhate et al. (2007) applied this definition and the optical boundaries it demarcates to the HI maps of their tidal tail sample to study the local column densities within. In M11, the expanded tidal tail sample afforded a glimpse at tails with different HI and optical morphologies, whose optically bright regions did not always coincide with accumulations of HI (c.f. Hibbard et al. 2000). Consequently, we redefine “in-tail” to refer to an area of the HI data that is confined to the WFPC2 footprint of its corresponding optical observations, and is either within the optical boundaries set by M11 or met the HI criteria of Section 3.1.

For each tail, we determine the physical extent of the HI emission by convolving a map of the integrated flux density with an artificial beam twice the size of the synthesized beam and masking out pixels that do not satisfy the minimum criterion for HI signal. We found that this technique successfully suppresses artifacts in the cube that are beyond the true large-scale emission in the tidal debris, as opposed to using no smoothing kernel or kernels of sizes  $\gtrsim 3$  times that of the beam. Regions determined to reside at the WFPC2-imaged edges of the host galaxies by M11 were rejected.

### 3.3. Measured Properties

#### 3.3.1. Primary Properties

The three-dimensional nature of the HI cubes provides an opportunity to examine not only the distribution of local HI surface densities, but also the velocities and kinematics of the gas. Thus, for each in-tail pixel, we compute the total integrated intensity  $I_{\text{tot}}$  ( $\text{Jy beam}^{-1} \text{ km s}^{-1}$ ), the mean line-of-sight velocity  $v_{\text{los}}$  ( $\text{km s}^{-1}$ ), and the line-of-sight velocity dispersion  $\sigma_{\text{los}}$  ( $\text{km s}^{-1}$ ). In each pixel, we calculate  $I_{\text{tot}}$  as the zeroth moment of the velocity-intensity distribution:

$$I_{\text{tot}} = \sum_{i=1}^N I_i dv, \quad (1)$$

where  $I_i$  is the intensity in each signal channel and  $dv$  is the channel width in  $\text{km s}^{-1}$ . Again, The corresponding integrated flux density  $S_{\text{tot}}$  can be obtained by multiplying  $I_{\text{tot}}$  by the ratio of pixel and beam angular sizes  $A_{\text{pix}} A_{\text{beam}}^{-1}$  (both in  $\text{arcsec}^2$ ). The line-of-sight velocity and (squared) velocity dispersion is given by the first and second moments:

$$v_{\text{los}} = \frac{1}{N} \frac{\sum_{i=1}^N v_i I_i}{\sum_{i=1}^N I_i}, \quad (2)$$

and:

$$\sigma_{\text{los}}^2 = \frac{1}{N} \frac{\sum_{i=1}^N (v_i - v_{\text{los}})^2 I_i}{\sum_{i=1}^N I_i}, \quad (3)$$

respectively. In Equation (2) and (3),  $v_i$  is the velocity value for the  $i$ -th channel. Summations were performed only on channels left unmasked as described in Section 3.1–3.2 for all equations, and errors in  $I_i$  ( $\epsilon_{I_i}$ ) were propagated through to all quantities. We adopt a minimum value of 50% of the given channel width for  $\sigma_{\text{los}}$  (an instrumental limit), as well as for errors in both  $v_{\text{los}}$  and  $\sigma_{\text{los}}$ . For pixels defined as in-tail by virtue of their optical properties alone, these moments were not computed and the HI properties were classified as “unfitted.” In occasional cases of marginally detectable HI emission (a moment-zero measurement), higher moments were unable to be reliably

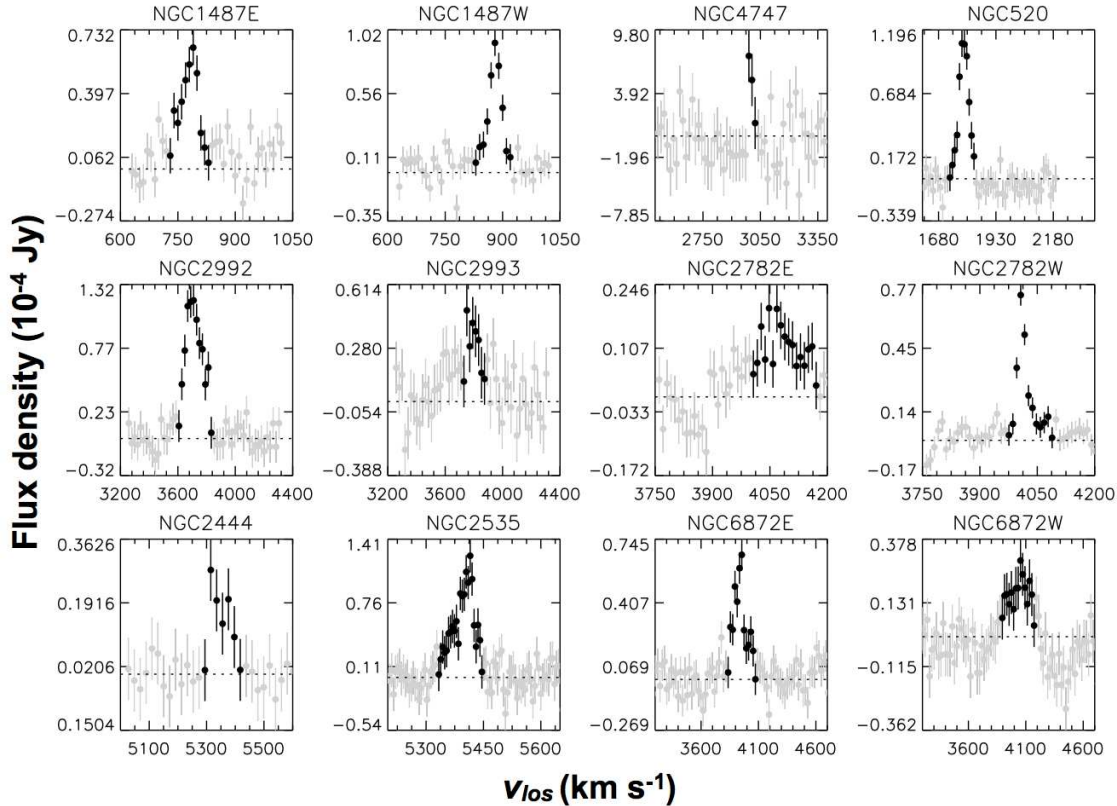


Fig. 1.— Randomly selected example spectra of pixels in the HI debris of NGC 1487E–NGC 6872W. Gray points indicate data for all channels; black points indicate channels that have been selected as HI emission with the criteria and procedure of §3.1. Error bars (r.m.s. noise) are also shown.

determined, and such pixels were therefore unfit in  $v_{\text{los}}$  and  $\sigma_{\text{los}}$ .

For visual reference, we display moment-zero integrated flux density maps of the full extent of each data cube in Figure 3, with WFPC2 fields of view overlaid. In all images, north is up, east is to the left of the frame, and every WFPC2 footprint is  $\approx 2'.47$  on a side. The sizes and orientations of the synthesized radio beams are represented in the bottom left of each frame in this figure.

We also experimented with finding the equivalent quantities by fitting the HI spectra offered by each pixel with a series of gaussian functions. In practice, we found that our values of  $S_{\text{tot}}$  for both methods agreed very well. However, spectral fitting often yielded multiple gaussian components, so in many cases it could not be easily determined which component was “best” associated with the tidal debris and which  $v_{\text{los}}$  and  $\sigma_{\text{los}}$  should be com-

pared to the moment equivalents (c.f. the complex line structures evinced in Figures 1–2). The intensity-weighted mean of the individual components facilitated a comparison of the  $v_{\text{los}}$  measurements, but there was no clear prescription for comparing the number of  $\sigma_{\text{los}}$  contributions from the gaussian fits to the moment-based measurement. Many pixels throughout the tail sample can be well fit by multiple gaussian components that overlap in varying amounts, so summing the gaussian-fit velocity dispersions would be an inaccurate universal tracer of kinematic complexity.

In all, because the results for integrated flux density were very similar, and for simplicity of analysis we wish to use single quantities to describe the velocity structure at positions along a tidal tail, we choose to employ the moment measurements for these primary properties. Similar work for galaxy disks can be found in

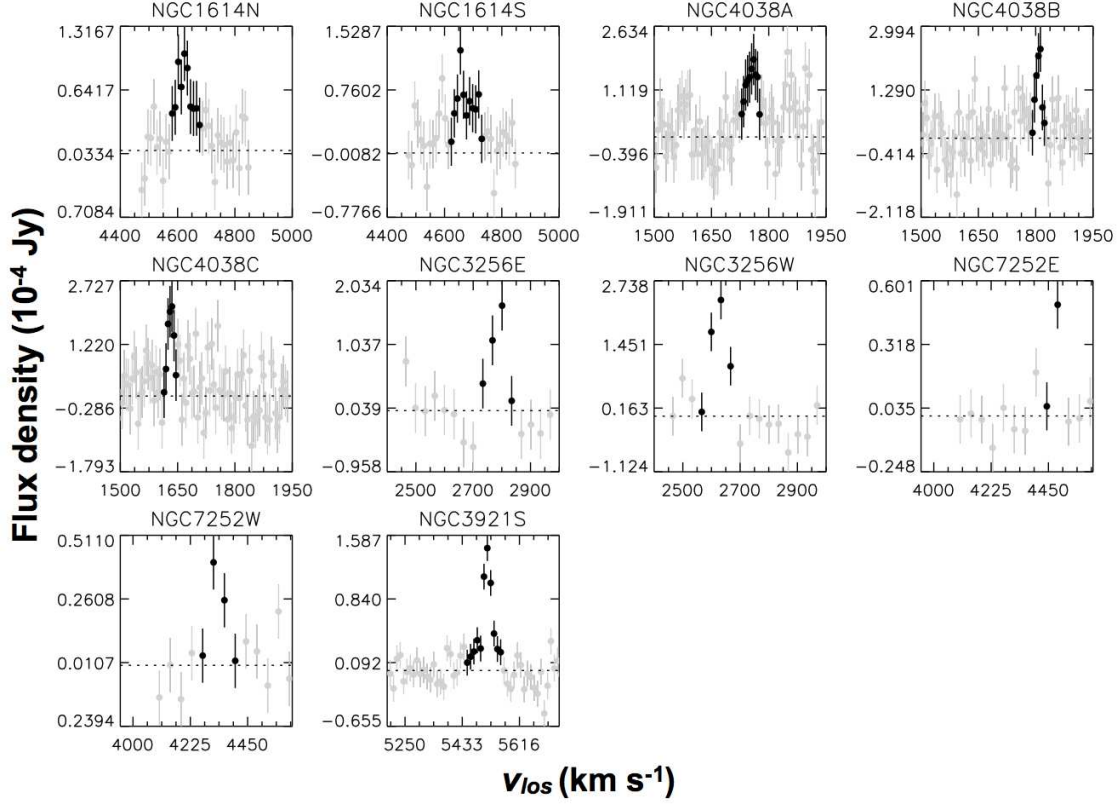


Fig. 2.— Randomly selected example spectra of pixels in the HI debris of NGC 1614N–NGC 3921S. Gray points indicate data for all channels; black points indicate channels that have been selected as HI emission with the criteria and procedure of §3.1. Error bars (r.m.s. noise) are also shown.

Tamburro et al. (2009). While this method loses sight of interesting kinematics in some locations along tidal tails, e.g. multiple overlapping gaussian fits and extended or asymmetric profiles, complex line structures are still reflected in large second moments of the intensity distributions. Our measurement of  $\sigma_{\text{los}}$  is thus still a tracer of such tail HI kinematics.

### 3.3.2. Secondary Properties

Further HI characteristics can be calculated from the moment-based primary properties, e.g., the HI column density, mass surface density, and large-scale velocity gradient. The total integrated intensity  $I_{\text{tot}}$  is related to the HI column density  $N_{\text{HI}}$  ( $\text{cm}^{-2}$ ) by the simplified relation (e.g., Verschuur & Kellermann 1988):

$$N_{\text{HI}} [\text{cm}^{-2}] = 1.247 \times 10^{24} \frac{I_{\text{tot}}}{A_{\text{beam}}} . \quad (4)$$

Here,  $A_{\text{beam}}$  is the area of the beam in square arcseconds. The error in  $N_{\text{HI}}$  is given by:

$$\epsilon_{N_{\text{HI}}} [\text{cm}^{-2}] = 1.247 \times 10^{24} \frac{\sqrt{N_{\text{u}}}}{A_{\text{beam}}} \epsilon_{I_i} dv . \quad (5)$$

$N_{\text{u}}$  denotes the number of unmasked channels for the specified pixel,  $dv$  is the channel width ( $\text{km s}^{-1}$ ), and  $\epsilon_{I_i}$  is the single channel r.m.s. error in  $I_i$ . The corresponding error in  $S_i$  ( $\epsilon_{S_i}$ ) is then simply  $(A_{\text{pix}} A_{\text{beam}}^{-1}) \epsilon_{I_i}$ .

We moreover measure the mass surface density, kinetic energy density, and velocity gradient of each pixel. The mass surface density  $\Sigma_{M_{\text{HI}}}$  and its uncertainty  $\epsilon_{\Sigma_{M_{\text{HI}}}}$  are calculated with the following equations (from Verschuur & Kellermann 1988, with some alterations to change masses to mass surface densities and include unit conver-

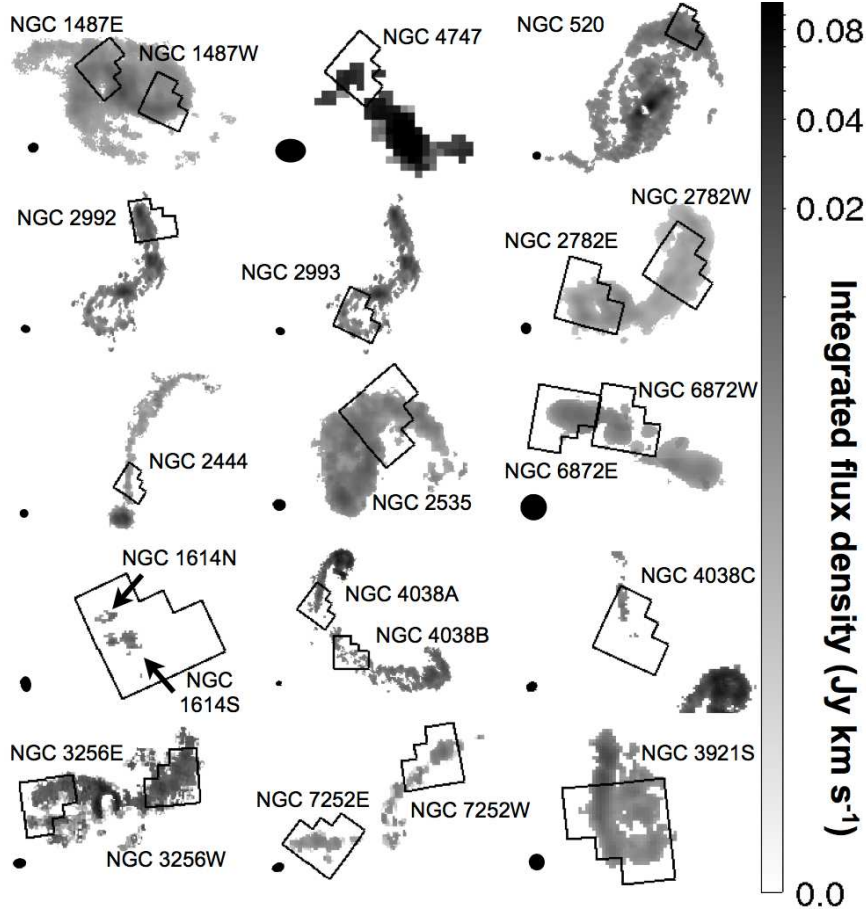


Fig. 3.— Channel-integrated flux density maps of the tidal tails of our sample (see Figure 1 of M11 and K03 for optical counterparts). WFPC2 FOVs are overlaid as black footprints; these are all  $\approx 2'47$  on a side. The sizes and orientations of the synthesized radio beams are represented in the bottom left of each frame. A full resolution version of this figure is available in *The Astrophysical Journal*.

sions):

$$\Sigma_{M_{\text{HI}}} [M_{\odot} \text{ pc}^{-2}] = 1.00 \times 10^4 \frac{I_{\text{tot}}}{A_{\text{beam}}}, \quad (6)$$

and:

$$\epsilon_{\Sigma_{\text{MHI}}} [M_{\odot} \text{ pc}^{-2}] = 1.00 \times 10^4 \frac{\sqrt{N_{\text{u}}}}{A_{\text{beam}}} \epsilon_{I_i} dv, \quad (7)$$

where  $\epsilon_{I_i}$  is the single channel r.m.s. error in intensity as above.

To characterize the dynamical state of the HI gas, we further define the kinetic energy density of the gas in a single pixel as  $\Sigma_{\text{KE}} = \alpha \Sigma_{M_{\text{HI}}} \sigma_{\text{los}}^2$ , where the factor  $\alpha=3/2$  assumes the velocity distribution is isotropic. Tamburro et al. (2009) similarly calculate a pixel-by-pixel kinetic energy for

their sample of non-interacting galaxies. For streaming HI features at a variety of inclinations and projection effects, this constant may differ in reality by a factor of a few. Thus we consider this only an order-of-magnitude tracer of the actual, local turbulent kinetic energy per unit area.

Lastly, we produce a diagnostic of the locally centered line-of-sight velocity gradient across the plane of the sky  $dv_{\text{los}}/dr_{\perp}$  ( $\text{km s}^{-1} \text{ kpc}^{-1}$ ) from the root mean square of the velocity gradients between the pixel of interest and others in its imme-

diate neighborhood. We write this as:

$$dv_{\text{los}}/dr_{\perp} = \frac{1}{\sqrt{N_{\text{pix}}}} \left( \sum_{i=1}^{N_{\text{pix}}} \frac{(v_i - v)^2}{dr_{\perp,i}^2} \right)^{\frac{1}{2}}, \quad (8)$$

where  $v$  is the HI velocity for the central pixel of interest and  $v_i$  is the equivalent velocity for the  $i$ -th nearby pixel with which we construct a velocity gradient over  $dr_{\perp,i}$ , the distance in kpc between the pixels.  $N_{\text{pix}}$  is the number of pixels that surround the central pixel of interest and are used in the calculation. Here, we use all pixels with measurable HI emission that surround the central pixel in an annulus whose inner and outer radii are set by 0.5 and 1.5 times the maximum dimension of the beam. This allows a comparison between the central pixel of interest and the closest statistically uncorrelated pixels 1 beam away. Thus, while previous quantities pertain to pixel scales ( $\sim$ kpc), this velocity gradient is measured over several beams, and probes gas motions and kinematics on larger ( $\sim$ 10 kpc) scales. If  $v_{\text{los}}$  and  $\sigma_{\text{los}}$  were unable to be determined in a given pixel, then that pixel was also deemed “unfitted” by  $dv_{\text{los}}/dr_{\perp}$ .

As an example of these calculations, we present a montage of  $N_{\text{HI}}$ ,  $\Sigma_{M_{\text{HI}}}$ ,  $\sigma_{\text{los}}$ , and  $v_{\text{los}}$  maps in Figure 4 for the tail NGC 2535. Corresponding maps of the remaining tail sample can be found in full resolution in the Online Figure Set 4. As before, we include the WFPC2 FOV, but also indicate positions of SCCs with circles. We furthermore introduce maps of  $\Sigma_{\text{KE}}$  and  $dv_{\text{los}}/dr_{\perp}$  in this figure. Contours of  $\log N_{\text{HI}}$  from 20.0 to 21.4 ( $\text{cm}^{-2}$ ) in steps of 0.2 dex are overlaid in all maps.

#### 4. Relating HI and SCC Distributions

Our motivation in this section is to determine whether there are observable environmental differences between regions of tidal tails that foster star cluster formation and those that do not, specifically to the best resolution each data set affords. For each tail we therefore separated HI pixels by their proclivity for harboring SCCs and compare their distributions of properties measured in Section 3. By contrasting the distributions of properties of tail pixels that contain no SCCs with tail pixels that contain at least one SCC, we assess

possible environmental differences on a  $\sim$ kpc scale within a given tail.

However, we realize that not all SCCs are star clusters, and some care must be taken in interpreting differences or similarities between HI characteristics for these two categories. Fortunately, if there are quantifiable differences between pixels with SCCs and those without despite contamination from non-cluster carrying pixels, these are still likely substantial indicators of environmental dissimilarity. Null results, given this caveat, are not as easily understood.

We reiterate that the pixel size across the sample is not a constant fraction of the beam sizes. Because we are not yet concerned with rigorously comparing the tails (that is deferred to Section 5), this is not an immediate concern. Rather, because the resolution remains set by the beam size, variations in pixel size for a given tail only affect the coarseness of any considered distribution of an HI property and not the distribution itself. Our plots of tail properties we discuss later in this section and the Appendix use bin sizes that are larger than the pixel-to-pixel variations between correlated pixels, so these are not affected.

#### 4.1. Individual SCC-Harboring Probabilities

In this section, we concentrate on the pixels of a given tail that contain at least one SCC. The sources detected in M11 are not verified clusters, but cluster candidates, so each of these pixels has a probability that it contains at least one actual, luminous cluster. We therefore first examine the source statistics in a manner consistent with M11 to determine how likely a source is a cluster rather than a background contaminant. From this we compute the probability that the pixel containing that SCC has at least one cluster.

Similar to M11, we determine the relative areas within and outside the tail regions surveyed within the WFPC2 footprint,  $A_{\text{in}}$  and  $A_{\text{out}}$ , respectively. The main difference in this study, aside from pixel sizes, is the optical/HI tail definition used here. Within these areas, we find the number of SCCs  $N_{\text{in}}$  and  $N_{\text{out}}$ . We divide  $N_{\text{in}}$  by  $A_{\text{in}}$  to find the overall in-tail source density  $\Sigma_{\text{in}}$ ; these results are listed in Table 3 for each tail, along with the in-tail completeness limits found in M11.

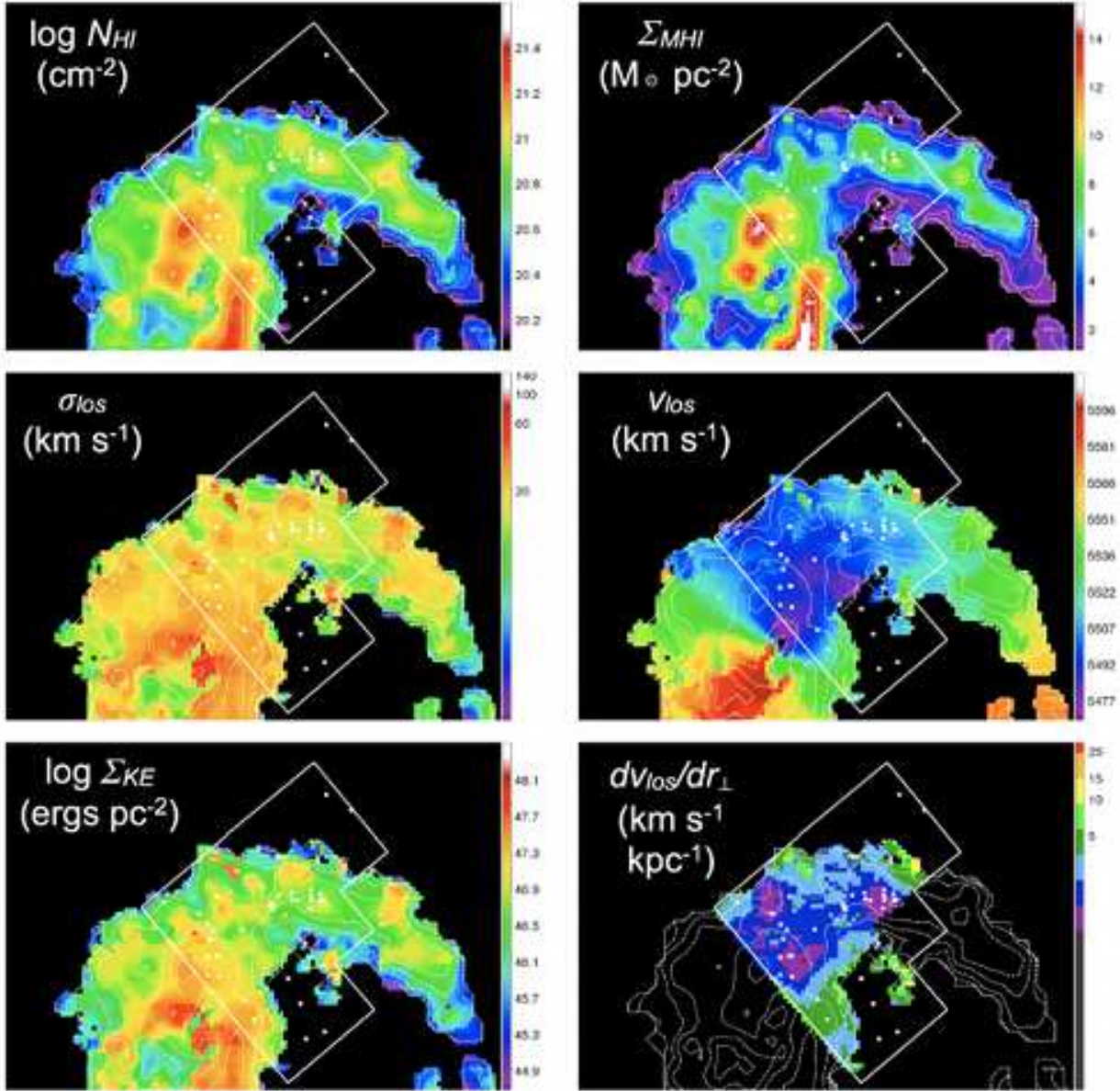


Fig. 4.— Maps of several derived quantities -  $N_{\text{HI}}$ ,  $\Sigma_{\text{MHI}}$ ,  $\sigma_{\text{los}}$ ,  $v_{\text{los}}$ ,  $\Sigma_{\text{KE}}$ , and  $dv_{\text{los}}/dr_{\perp}$  fit for the tail NGC 2535. Contours of  $\log N_{\text{HI}} = 20.0\text{--}21.4$  ( $\text{cm}^{-2}$ ) in steps of 0.2 dex are overlaid on all maps. Although we only consider pixels within the WF2–WF4 chips of the overlaid WFPC2 FOV, the rest of the system has been mapped for clarity in some cases. Full resolution Figures 4.1–4.22 for all tails are available in the electronic edition of *The Astrophysical Journal*.

M11 also calculated the out-of-tail density  $\Sigma_{\text{out}} = N_{\text{out}}/A_{\text{out}}$  and subtracted it from  $\Sigma_{\text{in}}$  to find the background-subtracted, average in-tail density of SCCs in these tidal tail regions. However, Table 3 shows that many, particularly close systems have extensive HI and optical coverage and small out-of-tail areas  $A_{\text{out}}$ . The number of detected out-of-tail objects within these regions is statistically uncertain, or not at all known ( $N_{\text{out}} = 0$ ) in some cases.

We therefore determine  $\Sigma_{\text{out}}$  with results from star counts generated by the Galactic population synthesis model of Robin et al. (2003)<sup>5</sup>. In a 100 arcsec<sup>2</sup> solid angle centered at coordinates in each tail, we generate the number of foreground stars visible within the photometric criteria of Section 2. This includes a  $V - I < 1$  cutoff and an apparent  $V$ -band magnitude range matching the sources detected in, and completeness limits of, M11 ( $19 \lesssim V \lesssim 26$ ). We then determine the resulting number of contaminants per out-of-tail area  $\Sigma_{\text{out}}$  using the distance to each tail. We find that variations of solid angle (1–100 arcsec<sup>2</sup>) introduce variations of only a few percent.

In this calculation, we also roughly model the photometric errors of the returned catalogs on the errors in photometry in M11. Here, errors in magnitude  $m$ ,  $\sigma_{\text{mag}}$  are calculated by a simple linear model  $\sigma_{\text{mag}} = A + Bm$ , where  $A$  and  $B$  are 0.01 and 0.0035, respectively. Moreover, we employ a mean  $V$ -band diffuse absorption of 0.7 mag kpc<sup>-1</sup>, which is recommended for intermediate-to-high Galactic latitudes (Robin et al. 2003). It should be noted that this may introduce some uncertainty for NGC 3256E/W, which is a particularly low-latitude ( $b \approx 11^\circ$ ) object. But ultimately, it is a more reliable method that is more free of statistical uncertainties with low counts of detected objects. In addition, these sources were screened for extended sources in M11, so contamination by background galaxies—already a minor issue from the stringent  $V - I$  cutoff—is minimal. In short, the primary contamination should be foreground stars, and this is better assessed with the current method.

We want to concentrate on individual in-tail SCCs and their local environments, so we then calculate the probability  $p_{\text{real}}$  that a SCC-containing

pixel contains at least one cluster based on the probable degree of in-tail contamination by out-of-tail sources. To do so we first find the area-adjusted number of probable contaminants in the in-tail source list,  $\Sigma_{\text{out}} \times A_{\text{in}}$ . This quantity divided by  $N_{\text{in}}$  is simply the fraction of sources within the tail that are likely contaminants, or  $\Sigma_{\text{out}}/\Sigma_{\text{in}}$ . The corresponding fraction of sources that are likely star clusters (SCs) is then  $f_{\text{SC}} = 1 - (\Sigma_{\text{out}}/\Sigma_{\text{in}})$ .

We record various steps of this process in Table 3, along with the calculated  $V$ -band 50% completeness limits for each tail (M11; Knierman et al. 2003; Maybhate et al. 2007) for reference. For pixels containing one SCC,  $p_{\text{real}}$  is just the value of  $f_{\text{SC}}$  for that tail. More generally, and especially for pixels with multiple SCCs,  $p_{\text{real}}$  is the result of applying the binomial distribution, using  $n$  SCCs in a pixel, each with a probability  $p_{\text{real}} = f_{\text{SC}}$ . Thus, the odds that a pixel with multiple SCCs has at least one actual cluster are higher than those listed for single SCC-harboring pixels listed in the penultimate column of Table 3. We indicate in the last column whether M11 found strong statistical evidence of tail-wide cluster population in each of the tail regions. With the exception of the low-latitude (and highly foreground source-contaminated) NGC 3256W,  $f_{\text{SC}}$  values are all  $\gtrsim 0.7$ . In contrast, tails without global cluster populations exhibit a wider range of values.

As a final check, we compared the distribution and properties of star clusters detected in NGC2782W by Torres-Flores et al. (2012) and M11. Because of the instrumental differences between the studies (the former use *GALEX* imaging and optical spectra, and the latter use *HST* imaging), there is  $\approx 50\%$  overlap between the source catalogs for that tail. That is, M11 detected about twice as many cluster candidates as Torres-Flores et al. (2012) spectroscopically characterized clusters. This agrees very well with results from the star counts model that predicted 52% of the M11 detections are contaminants.

## 4.2. Comparison of HI Distributions

We now compare the distributions of  $N_{\text{HI}}$ ,  $dv_{\text{los}}/dr_{\perp}$ ,  $\sigma_{\text{los}}$ , and  $\Sigma_{\text{KE}}$  for between HI pixels not containing SCCs and those that do. In doing so we must ignore the fraction of pixels that were unfitted by the measuring techniques,  $f_{\text{unfit}}$ ; these

<sup>5</sup><http://www.model.obs-besancon.fr>



**Table 3.**  
Source Statistics

Tail	Source Detections						Star Counts			M11 Results
	$M_{V,50\%}^a$	$N_{in}^b$	$N_{out}^c$	$A_{in}^d$	$A_{out}^e$	$\Sigma_{in}^f$	$\Sigma_{out}^g$	$\Sigma_{out} \times A_{in}^h$	$f_{SC}^i$	Tail-wide SCCs? <sup>j</sup>
NGC 1487E	-4.6	1	0	40.60	5.89	0.025	0.039	1.56	0	
NGC 1487W	-4.5	0	0	41.07	5.52	0	0.039	1.58	1	
NGC 4747	-6.0	6	1	84.52	84.52	0.071	0.014	1.22	0.80	
NGC 520	-6.4	2	0	266.21	28.66	0.008	0.007	1.87	0.06	
NGC 2992	-7.2	10	3	305.49	229.87	0.033	0.009	2.77	0.72	✓
NGC 2993	-7.3	11	1	367.49	169.38	0.030	0.009	3.34	0.70	✓
NGC 2782E	-7.5	56	5	413.93	165.16	0.135	0.006	2.50	0.96	✓
NGC 2782W	-7.3	6	2	472.48	105.25	0.013	0.006	2.85	0.52	
NGC 2444	-8.2	5	7	504.38	850.42	0.010	0.004	1.83	0.63	
NGC 2535	-8.4	36	8	871.95	554.81	0.041	0.003	2.36	0.93	✓
NGC 6872E	-8.3	111	28	730.59	824.29	0.152	0.009	6.68	0.94	✓
NGC 6872W	-8.5	101	14	729.12	827.22	0.139	0.009	6.66	0.93	✓
NGC 1614N	-8.6	19	8	304.89	1408.86	0.062	0.003	1.01	0.95	✓
NGC 1614S	-8.6	30	10	325.82	1387.93	0.092	0.003	1.07	0.96	✓
NGC 4038A	-5.8	3	0	45.79	30.30	0.066	0.050	2.30	0.24	
NGC 4038B	-5.1	1	0	46.91	29.96	0.021	0.050	2.35	0	
NGC 4038C	-5.8	1	0	27.50	48.71	0.036	0.050	1.38	0	
NGC 3256E	-7.8	32	9	460.19	271.43	0.070	0.035	16.12	0.50	
NGC 3256W	-7.8	51	4	580.74	146.74	0.088	0.035	20.34	0.60	✓
NGC 7252E	-8.1	11	16	627.03	928.00	0.018	0.003	2.18	0.80	
NGC 7252W	-8.1	17	11	533.54	1016.92	0.032	0.003	1.85	0.89	
NGC 3921S	-8.8	14	5	1718.82	1147.28	0.008	0.001	1.79	0.87	

**Notes.**

<sup>a</sup>50% V-band completeness limit (M11)

<sup>b</sup>Number of SCCs detected within the tail region

<sup>c</sup>Number of SCC-like objects detected outside the tail region

<sup>d</sup>Area of in-tail region (kpc<sup>2</sup>)

<sup>e</sup>Area of out-of-tail region (kpc<sup>2</sup>)

<sup>f</sup>In-tail SCC surface density (kpc<sup>-2</sup>)

<sup>g</sup>Out-of-tail surface density of SCC-like objects (kpc<sup>-2</sup>)

<sup>h</sup>Probable number of in-tail SCCs that are contaminants

<sup>i</sup>Overall fraction of SCCs that are likely star clusters

<sup>j</sup>This column is checked if M11 found evidence for large-scale populations of star clusters within the tail regions

are typically pixels that fall within the *optical* tail, but have ill-defined HI content. To outline potential contrasts between the pixels that are home to potential star clusters and those that are not, we performed K–S tests between these distributions for each measured property. Here,  $p_{KS}$  values reveal the probability that the SCC-sporting and SCC-empty pixels come from the same distribution of each measurement. If  $p_{KS} \lesssim 0.01$ , it is likely that these two categories of pixels have two separate distributions of an HI characteristic. The results of these tests are also provided in Table 4; columns indicate the results of this test performed on the indicated property. We indicate where values are below  $10^{-4}$ , as specific results below this cutoff are not enlightening.

Overall, it appears that the distributions of our calculated HI column densities, kinematic trac-

ers, and mechanical energy densities for both SCC-carrying and SCC-devoid pixels are indistinct ( $p_{KS} \gtrsim 0.01$ ). NGC 2782E and NGC 6872E are remarkable counterexamples, with low computed K–S probabilities and two of the highest tail-wide SCC population densities reported in M11 ( $\approx 0.2$  SCCs kpc<sup>-2</sup>). A few other tails show evidence of independent distributions of individual properties between these two pixel types (e.g., NGC 2992 with  $N_{HI}$ , NGC 2535 and NGC 6872W with  $dv_{los}/dr_{\perp}$ , and NGC 3256E and NGC 7252W with  $\sigma_{los}$ ). The implications of these results are discussed for individual tails in the Appendix. It is probable that the varying degree of contamination from foreground stars across the tail sample—displayed in Table 3—contributes to a contamination of the HI distributions for the pixels hosting at least one SCC and confuses the K–S results.

It is additionally important to consider that there are minor, inherent shortcomings to K–S tests; namely that they are particularly sensitive to differences in the centers of cumulative distribution functions relative to their edges. Also note that many tails have small samples of SCC-carrying pixels, to which such statistical tests are particularly sensitive. As mentioned at the outset of this section, pixel size variations also introduce differences in the number of pixels considered, and the coarseness of the unbinned HI measurement distributions. This will have some, albeit minor, affect on the results of the K–S tests.

With all uncertainties considered, two distributions with K–S probabilities  $\gtrsim 0.01$  may still be independent but are difficult to differentiate here. Regardless, it appears that the dependence of star cluster positions (and possibly clues to their formation) on individual HI densities and kinematics cannot be easily ascertained on a tail-by-tail, property-by-property basis like this. We therefore also explore the holistic HI parameter space of the tail pixels, to see if and how all these HI properties collectively relate to SCCs. Figure 5 shows the combined distributions of  $N_{\text{HI}}$  and  $\sigma_{\text{los}}$  (left), and  $\Sigma_{\text{KE}}$  and  $dv_{\text{los}}/dr_{\perp}$  (right) of NGC 2535. Similar plots for the remaining tail sample are available in the Online Figure Set 5. Bin sizes of 0.1 dex in  $\log N_{\text{HI}}$  ( $\text{cm}^{-2}$ ),  $5.0 \text{ km s}^{-1}$  in  $v_{\text{los}}$ ,  $2.0 \text{ km s}^{-1} \text{ kpc}^{-1}$  in  $dv_{\text{los}}/dr_{\perp}$ , and 0.25 dex in  $\log \Sigma_{\text{KE}}$  ( $\text{erg pc}^{-2}$ ) were employed in contouring. Contour levels are scaled to show the fraction of the total number of tail pixels examined, including pixels that were unfitted by  $N_{\text{HI}}$ ,  $\sigma_{\text{los}}$ ,  $dv_{\text{los}}/dr_{\perp}$ , or  $\Sigma_{\text{KE}}$  measurements. We record the fraction of unfitted SCC-carrying and SCC-devoid pixels for reference as  $f_{\text{unfit}}^{\text{SCC}}$  and  $f_{\text{unfit}}$ , respectively. Median uncertainties for all unbinned properties are shown as red error bars.

Dashed lines in the first plot show potentially important values of the plotted properties—the Maybhate et al. (2007)  $N_{\text{HI}}$  threshold (horizontal line), and the turbulent–thermal transition  $\sigma_{\text{los}} \approx 10 \text{ km s}^{-1}$  (vertical line; this shows where gas velocity dispersions are driven by turbulent instead of thermal motions). The vertical dashed line on the second plot indicates a constant  $dv_{\text{los}}/dr_{\perp} = 15 \text{ km s}^{-1} \text{ kpc}^{-1}$ , approximately the value of the Oort constant A, the value of the shear in the solar neighborhood. This line is purely fiducial

and meant to guide distinctions between relatively shallow and steep velocity gradients. The horizontal line on that plot shows a  $\Sigma_{\text{KE}}$  cutoff of  $10^{46} \text{ erg kpc}^{-2}$ , which considers an energy threshold set by setting a hypothetical critical HI mass surface density for star formation of  $3 M_{\odot} \text{ pc}^{-2}$  (Schaye 2004) and threshold turbulent velocity dispersion  $10 \text{ km s}^{-1}$ . These demarcations are meant to guide the eye and highlight what fraction of a tail has relatively more dense, turbulent, etc. gas.

We indicate the fraction of the total number of tail pixels that exhibit super-“critical” HI characteristics for the combined distributions with  $f_{\text{gas}}^{\text{Q1}}$  for the left plot, and  $f_{\text{gas}}^{\text{Q2}}$  for the right. “Q1” and “Q2” refer to particular quadrants delineated by the dashed lines, i.e. gas with  $\log N_{\text{HI}} > 20.6 \text{ cm}^{-2}$  and  $\sigma_{\text{los}} > 10 \text{ km s}^{-1}$  (left plot), and gas with  $\log \Sigma_{\text{KE}} > 46 \text{ erg pc}^{-2}$  and  $dv_{\text{los}}/dr_{\perp} < 15 \text{ km s}^{-1} \text{ kpc}^{-1}$  (right plot). Lastly, the SCC-laden pixels are overplotted in both plots as gray points if their calculated  $p_{\text{real}}$  values are  $\leq 0.94$ , and as black points if  $p_{\text{real}} > 0.94$ . This value of 0.94 was selected with some foresight and will be addressed further in Section 5. Recall that  $p_{\text{real}}$  indicates the likelihood that an HI pixel contains at least one star cluster. The plots in Online Figure Sets 4 and 5 are discussed individually for each tail region in the Appendix.

A clear correlation is evident between HI column density and line-of-sight velocity dispersion for much of our sample as seen in Online Figure Set 5. The example spectra displayed in Figures 1 and 2 show that many of these randomly selected HI profiles are kinematically complex, and many would have wide velocity dispersions as measured by the second moment of the intensity distribution. The addition of multiple HI components therefore both broadens  $\sigma_{\text{los}}$  and increases  $N_{\text{HI}}$ . The degree of overlap between components in a spectrum may depend on the tail kinematics and projection effects, so we would perceive a different relationship—i.e. slope of contoured distributions—between these two properties in each tail of Figure Set 5. Most importantly, detecting multiple HI components indicates that the actual physical density of HI at the location of a pixel (or SCC) may not be consistently mapped by column density in all tails, so some confusion in interpreting the importance of  $N_{\text{HI}}$  is expected.

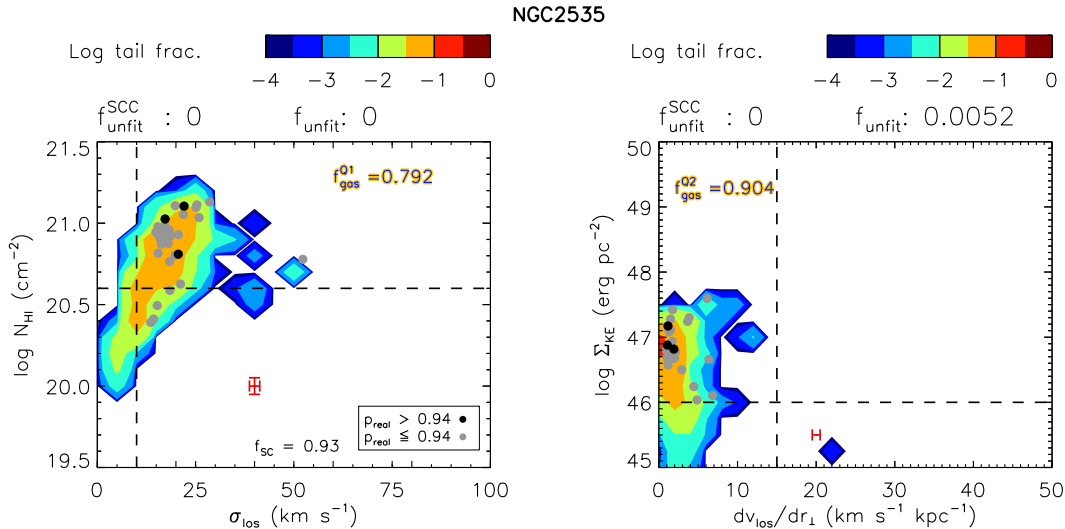


Fig. 5.— Combined, contoured distribution of measured HI quantities for NGC 2535, with levels corresponding to the fraction of the tail within the indicated parameter space. Pixels with SCCs most likely to have star clusters are plotted in black ( $p_{\text{real}} > 0.94$ ), and those less likely in gray ( $p_{\text{real}} < 0.94$ ). The number of unfitted pixels, and the tail fraction within the specified quadrants Q1 (left) and Q2 (right) are provided. These are defined by the intersection of lines of potential threshold column density (Maybath et al. 2007) with the thermal-turbulent velocity dispersion in the left plots; and their combined energy density with the value of shear in the solar neighborhood in the right plots. See §4 for details. Full resolution Figures 5.1–5.22 for all tails are available in the electronic edition of *The Astrophysical Journal*.

## 5. Results and Discussion

In the previous sections, we analyzed the HI properties to the best possible spatial resolution of their individual cubes. We present a thorough discussion of each tail’s results and figures in the Appendix. It is the purpose of that Appendix—and the supporting figures presented thus far—to review the SCC distributions and HI characteristics of each tail for the benefit of future work on individual tidal tails and the interplay between their ISM and their star cluster populations. Several intriguing qualitative trends in the  $\sim\text{kpc}$ -scale HI column densities, kinematics, and mechanical energy densities can be seen in this sample that would not be otherwise ascertained from the simple K–S tests of Table 4. These also help direct our approach in Section 5.1.

The most obvious trend to note is that several of the systems identified in M11 as having widespread cluster populations (reproduced as the last column of Table 3) also tend to have

a large fraction of their  $\sim\text{kpc}$ -scale HI with column densities exceeding the  $\log N_{\text{HI}} > 20.6 \text{ cm}^{-2}$  (NGC 2535, NGC 2782E, NGC 1614N/S, and NGC 3256W). This gas is also turbulent ( $\sigma_{\text{los}} \approx 10\text{--}75 \text{ km s}^{-1}$ ) with velocity dispersions that vary tail-to-tail, though probably in part because of tail orientation, projection effects, and spatial scales. Kinetic energy densities of the tails are therefore also generally high ( $\log \Sigma_{\text{KE}} > 46 \text{ erg pc}^{-2}$ ). The HI pixels with the highest probability of containing at least one cluster (and usually contain more than one SCC) very often lie in these high- $N_{\text{HI}}/\Sigma_{\text{KE}}$  regions; the selection of the  $p_{\text{real}}=0.94$  cutoff reflects this. Mechanical energy density should loosely trace HI pressures (i.e., integrated along the line of sight), so this would imply that large-scale clustered star formation as detected by M11 requires high pressures (high  $\Sigma_{\text{KE}}$ ) and high  $N_{\text{HI}}$  on the spatial scales probed here. Conversely, a number of tails with low numbers of SCCs and low calculated probabilities of their pixels containing real clusters have little high column

density and often also little observably turbulent gas (NGC 1487E/W if de-projected; NGC 4747, NGC 520, and NGC 4038ABC).

However, many tidal regions with large percentages ( $\gtrsim 50\%$ ) of their HI exhibiting high column densities and kinetic energy densities on these  $\sim$ kpc scales do not have pronounced cluster populations in M11 (e.g., NGC 2993, NGC 3256E, and NGC 2782W). In some cases tail orientations and projection effects may increase the observed  $N_{\text{HI}}$ , while the actual physical densities of HI may be low. Kinetic energy densities are also high from similarly inflated turbulent velocity dispersions ( $\sigma_{\text{los}} \approx 10\text{--}75 \text{ km s}^{-1}$ ). When compared to its eastern counterpart, NGC 2782W presents an interesting case for the hidden role of tail-wide  $\text{H}_2$  content or dust-to-gas ratios that may also account for the observed discrepancy in cluster formation efficiencies given similar atomic hydrogen content (these two tails can be easily compared because they are present in the same HI cube). The fact that NGC 2782E could be the distorted minor galaxy of the merger (Smith 1994) and has confirmed CO detections (Smith et al. 1999) would insinuate that the ISM is very different in these two tails. An existing molecular gas reservoir in one tail, and/or different dust-to-gas ratios among the debris regions would allow efficient star formation in one case but not another. Knierman et al. (2012) explore this concept further in their assessment of these tails.

Moreover, several tails have pixels with high probabilities ( $p_{\text{real}} > 0.94$ ) of containing at least one cluster in regions of low or undetected HI column density (NGC 4747, NGC 6872E/W, NGC 1614N/S). Either  $N_{\text{HI}}$  is not important for these tails (perhaps in concert with differing molecular content), it is important on physical scales smaller than we can currently resolve (note that these tails have some of the largest angular pixel and beam sizes of the sample), or it has been dispersed and/or consumed over  $\sim 100$  Myr timescales, after the clusters had formed. This is reasonably consistent with overall HI column density behavior with tail age seen in M11. Photoionizing feedback from local or central sources may also be a factor in these tails (e.g., Hibbard et al. 2000). Given our work with cluster probabilities, we also cannot say with certainty that many SCCs that lie in regions of low  $N_{\text{HI}}$  or  $\Sigma_{\text{KE}}$  are *not* clus-

**Table 4.**  
K–S Probabilities

Tail	$N_{\text{HI}}$	$\sigma_{\text{los}}$	$dv_{\text{los}}/dr_{\perp}$	$\Sigma_{\text{KE}}$
NGC 1487E	-	-	-	-
NGC 1487W	-	-	-	-
NGC 4747	-	-	-	-
NGC 520	-	-	-	-
NGC 2992	1.3e-3	0.10	0.52	0.23
NGC 2993	0.17	0.039	0.45	0.086
NGC 2782E	<1e-4	<1e-4	3.7e-4	<1e-4
NGC 2782W	0.80	0.43	0.67	0.33
NGC 2444	0.53	0.37	0.090	0.61
NGC 2535	0.012	0.15	9.6e-4	0.039
NGC 6872E	<1e-4	<1e-4	0.076	<1e-4
NGC 6872W	0.24	0.26	9.8e-3	0.33
NGC 1614N	-	-	-	-
NGC 1614S	0.93	0.39	0.017	0.89
NGC 4038A	-	-	-	-
NGC 4038B	-	-	-	-
NGC 4038C	-	-	-	-
NGC 3256E	0.71	<1e-4	0.15	0.61
NGC 3256W	0.16	0.28	0.011	0.77
NGC 7252E	0.99	0.50	0.63	0.99
NGC 7252W	0.42	7.7e-3	0.044	0.39
NGC 3921S	0.41	0.27	0.87	0.25

ters (e.g., NGC 7252 and NGC 2444). Feedback, interaction dynamics, and gas dispersal may again have had an effect here, or these tails may be home to smaller-scale star formation events producing few bound, luminous clusters as opposed to the large-scale triggered events our study is better designed to address.

A few tails may also highlight the importance of velocity gradients on larger scales. A number of tails show large regions of locally, relatively shallow  $dv_{\text{los}}/dr_{\perp}$  (values vary from the size of the beam and the velocity structure of the HI). In several cases these are areas of many different beam physical scales where many SCCs are located (NGC 2992, NGC 3256W, NGC 6872E, NGC 2535, NGC 2782E, and NGC 7252W), or there is a prominent, diffuse optical structure that may have lower mass star clusters (NGC 1487E/W). This possibly underscores the importance of large-scale ( $\sim 10$  kpc) kinematics in star cluster formation, including tail-wide shearing motions (and lack thereof) that our measurement of the line-of-sight velocity gradient might trace in certain tails.

These results are promising, but we again caution against more rigorously comparing the HI distributions between the debris regions as shown thus far. These tails exhibit a large morphological diversity, both from their range of interaction stages and types, and also intractable projection effects from inclination and their orientation on

the sky. Models show that tails can have a wide range of both small- and large-scale thicknesses along our line of sight (Smith 1994); thus surface densities and other properties discrepant by a factor of  $\sim 3$  can all correspond to one “in-tail” physical density. Highly inclined mergers can also dramatically increase the apparent thickness of a tail. We see this especially with NGC 1487 and NGC 2992, where, for many pixels, their “true”  $N_{\text{HI}}$  values may be lower by an order of magnitude.

The translation of other line-of-sight properties to true physical properties might be even more complicated. If the local velocity dispersions within tails are not always isotropic (and they are certainly not likely to be), the proper interpretation of  $\sigma_{\text{los}}$  will vary pixel-to-pixel. Streaming motions of multiple HI components along our line-of-sight and beam smearing along the plane of the sky will further affect our measurements of  $\sigma_{\text{los}}$ , not to mention  $dv_{\text{los}}/dr_{\perp}$ . That quantity bears the additional warning that artificial pixel-to-pixel variations that arise in trying to define  $v_{\text{los}}$  in a region of low HI signal (the tail boundaries) will produce high  $dv_{\text{los}}/dr_{\perp}$  values. This is seen in a few tails in Figure Sets 4 and 5. Furthermore,  $\Sigma_{\text{KE}}$  is defined as an isotropic energy density, which is a less accurate description of the actual dynamic state of the HI gas as beam smearing and ordered gas motions becomes more prominent.

Table 3 furthermore reveals that several especially distant tails suffer from completeness effects, and our source lists for them are incomplete by 50% or slightly more. In these cases, all pixels have a slightly higher probability that they contain an SCC, with different adjustments for the different completeness curves of in-tail and out-of-tail areas. The completeness curves of M11 show that out-of-tail areas are complete to fainter magnitudes than in-tail regions (by  $\sim 0.5$  mag); thus for a source luminosity bin close to the completeness limits, we are likely to detect more sources out of tail than in-tail in distant systems. By this logic our computed contamination fractions are overestimated, and the  $p_{\text{real}}$  probabilities for SCC-carrying pixels derived from  $f_{\text{SC}}$  fractions listed in Table 3 are too low. Since this effect does not artificially increase the probability that pixels with SCCs contain observable clusters, we consider our existing  $p_{\text{real}}$  work to be suitable lower limits.

Lastly and most importantly, a cursory glance at Table 1 reveals that, by necessity, data from these tails are quite heterogenous. They arise from a number of different observation program designs, array configurations and weightings in the reduction process, and therefore exhibit a range of output channel widths and pixel/beam sizes. Not all tails are sensitive to the same velocity dispersions and physical scales, so additional care must be taken in assessing gas properties and possible thresholds across the tail sample more homogeneously.

### 5.1. Comparing HI, Global SCC Populations, and Interaction Characteristics

In this section we address the issue of heterogeneous physical resolution in our HI data and facilitate a better comparison between the tails in our sample. To make our HI cubes uniform in pixel scale, we repeated the work of Section 3–4 for the tails, but with their cubes re-gridded to the largest physical scale of the tail sample, i.e. the 2.1 kpc pixel scale of NGC 3921S. We exclude the NGC 6872E/W tails in this analysis, as their physical beam sizes ( $\approx 16$  kpc) are much larger than the rest of the sample (several kpc) and probe HI gas on correspondingly different spatial scales.

For this task, we used the IDL function *frebin*, which conserves flux for every spatial slice of the cubes. In all calculations requiring the beam size, the beam dimensions of each original cube was used, with the exception of the calculation of  $dv_{\text{los}}/dr_{\perp}$  (Equation (8)). Here, we used an annulus whose inner and outer radii are 4 and 12 kpc in the determination of  $N_{\text{pix}}$ . This simulates using an 8 kpc beam, which is physically the size of the largest beams in the sample (excluding NGC 6872E/W) and allowed a more direct comparison across the tail sample.

We then sorted all the analyzed tail pixels into two categories based on pertinent characteristics of the interactions—pixels from the list of tails with widespread cluster populations as determined by M11 vs. those from the tails that did not, pixels from tails that resulted from early-stage and late-stage interactions, and pixels from tails produced in interactions from different mass ratios of their progenitor galaxies. This approach allows a more significant assessment of HI and merger properties with respect to cluster populations than

additional individual studies would allow, especially for the closest half of the tail sample where the large physical pixel scales prohibit meaningful individual study. In the subsections below we therefore discuss these distinctions and the distributions of HI properties in greater detail, accompanying Figures 6–11.

In Figures 6, 8, and 10, we outline the normalized distributions of  $N_{\text{HI}}$ ,  $dv_{\text{los}}/dr_{\perp}$ ,  $\sigma_{\text{los}}$ , and  $\Sigma_{\text{KE}}$  for pixels from these types of tails. Subcategories of SCC richness, age, and mass ratio are represented as blue, filled histograms, and orange, outlined histograms. Cumulative distributions of these pixels are plotted over the histograms as blue and orange curves, respectively. In all cases, bin sizes were set by the number of pixels in each tail, and the standard deviation of their various distributions. We also indicate the fraction of pixels that were unfitted by the measuring techniques as  $f_{\text{unfit}}$ ; as before these are typically pixels that fall within the *optical* tail, but have ill-defined HI content.

We also perform K–S tests between the (unbinned) blue and orange distributions in each panel of these plots. In *all* cases we calculate extremely low probabilities ( $p_{\text{KS}} < 10^{-4}$ ) that these pairs of distributions are statistically indistinguishable. Thus, the differences in HI properties between tail types we note below are likely real and significant.

Figures 7, 9, and 11 are meanwhile analogous to the contour plots of Online Figure Set 5, excluding the presentation of  $f_{\text{SCC}}$ , which changes tail-to-tail. Individual pixel  $p_{\text{real}}$  probabilities were computed as before for each pixel containing at least one SCC from each tail and are reflected here. The fraction of unfitted SCC-carrying pixels  $f_{\text{unfit}}^{\text{SCC}}$  is also shown. Contour bins are also the same as in Figure 5, as are all definitions of HI thresholds. In each of these figures, we juxtapose the  $N_{\text{HI}}-\sigma_{\text{los}}$  and  $\Sigma_{\text{KE}}-dv_{\text{los}}/dr_{\perp}$  parameter space of the two types of tails considered for visual comparison.

In the following subsections, it is important to note that projection effects are still an issue. However, a reasonably random set of tail orientations would artificially change values of properties by different amounts and blur distinctions between distributions of an HI variable between two types of tails. We therefore contend that, while statistically similar distributions may be inconclusive

about physical differences between types of debris, statistically different distributions are still significant even against irrevocable geometric effects. Any differences between tail types are likely telling of real physical dissimilarities in the HI content between them.

### 5.1.1. HI and Tail-wide SCCs

Of the M11/Knierman et al. (2003) tail sample with HI coverage, M11 identified significant tail-wide cluster populations (to  $2.5\sigma$  confidence) in NGC 2993, NGC 2782E, NGC 2535, NGC 6872E/W, NGC1614N/S, and NGC 3256W. While NGC 2992 did not have a strictly global SCC population, many of its cluster candidates are found towards the tip of the optical tail, implying (along with their photometry and present statistics) that many could be real clusters. Therefore, we include that system along with the rest of those listed as tails with very likely widespread cluster populations. We therefore compared the HI properties of the re-gridded pixels of these tails with the remaining, globally SCC-poor, tail sample as in Section 4.2.

We present the results of this investigation in Figure 6, with solid blue and empty orange normalized histograms representing pixels from SCC-poor and SCC-rich tails, respectively. Most strikingly, the distributions of  $N_{\text{HI}}$  and  $\Sigma_{\text{KE}}$  are very clearly different between putatively cluster-rich and cluster-poor tails—the former peaks at about 0.5 dex higher in  $N_{\text{HI}}$  than the latter, with large percentage of its measurable HI pixels above the Maybhate et al. (2007) threshold. Tails with large numbers of SCCs also on average have higher HI kinetic energy densities on  $\sim\text{kpc}$  scales (again, by  $\sim 0.5$  dex). Despite individual cases of localized, probable clusters in tails with low column densities ( $\approx 20\%$  of the pixels of SCC-rich tails are unfitted for individual HI properties, compared to  $\approx 10\%$  for SCC-poor tails),  $N_{\text{HI}}$  and  $\Sigma_{\text{KE}}$  are still apparently important variables in the holistic appraisal of tidal tail cluster formation activity. These variables could be tied to physical HI densities and pressures, which likely play prominent roles in the formation of star clusters and other bound structures (e.g., Elmegreen 1993; Elmegreen & Efremov 1997; Elmegreen 2008).

Similarly, SCC-rich tails have an extended distribution of  $\sigma_{\text{los}}$ , with many pixels showing values

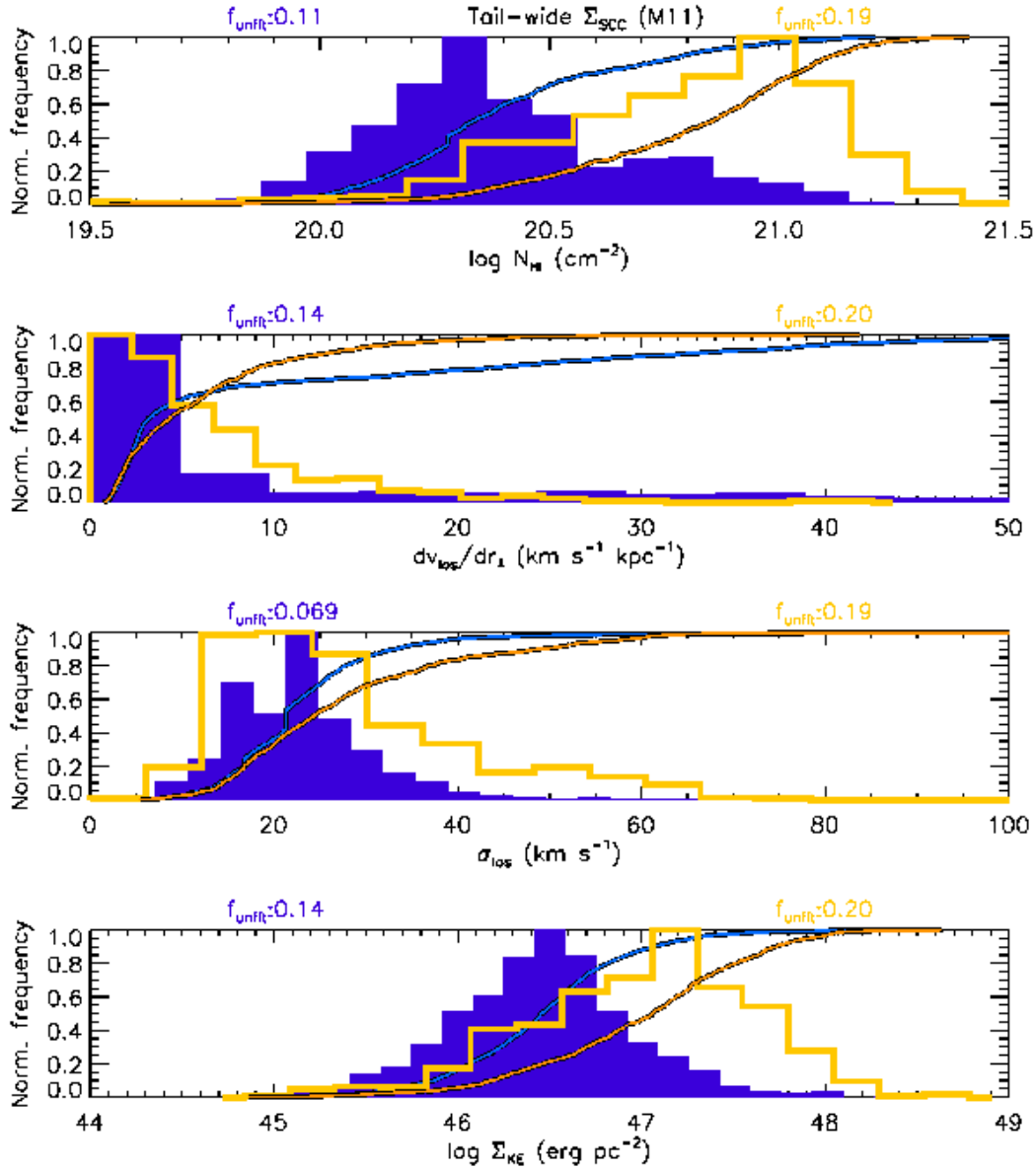


Fig. 6.— Normalized histograms of  $N_{\text{HI}}$ ,  $dv_{\text{los}}/dr_{\perp}$ ,  $\sigma_{\text{los}}$ , and  $\Sigma_{\text{KE}}$  for identically-sized pixels from tails that do not have global SCCs populations (blue) and those that do (orange). The fraction of unfitted pixels  $f_{\text{unfit}}$  is also recorded (see §5.1.1 for details). A full resolution version of this figure is available in *The Astrophysical Journal*.

in the 30–75 km s<sup>-1</sup> range. These tails seem to have more highly disturbed gas. While relatively more HI in SCC-poor tails appears to have line-of-sight velocity gradients  $\lesssim 10$  km s<sup>-1</sup> kpc<sup>-1</sup>, the velocity gradient measurement distribution trails off to generally higher values than that of the SCC-rich tails. This is also evident in contrasting the contour plots of Figure 7; the top row displays the contoured distributions for SCC-rich tails, and the bottom row the equivalent plots for SCC-poor tails. While about 60% of SCC-rich tail HI is measurably turbulent and of high column density, the percentage for the SCC-poor tails is only about 20%.

Understandably, SCC-rich tails have more over-plotted points than SCC-poor tails, and especially more pixels containing high probability clusters. Again, many of the highest probability clusters lie in regions of high column and kinetic energy density. However, as noted in the Appendix, many tails have probable clusters in unfitted or low-N<sub>HI</sub> pixels. Given the statistics of many of the sources, it is likely that many of the gray points also indicate positions of real clusters in this HI parameter space. Evidently, these plots provide a compelling argument for the importance of kpc-scale HI in tidal tail star cluster formation as a whole, but there are individual exceptions to the rule.

### 5.1.2. HI and Tail Dynamical Age

There is much evidence that tail age or interaction stage has a pronounced effect on star formation phenomenology. In their sample of compact groups, Martinez-Badenes et al. (2012) find evidence for a general decrease of molecular gas deficiency with the evolutionary phase (age) of the interacting group. They interpret this as an enhanced conversion of atomic to molecular gas early in the interactions, followed by gradual stripping and dispersal of HI in their later phases. In their models of compressive tides in pairwise galaxy mergers, Renaud et al. (2009) additionally show that, while regions with tidal compression can appear in interactions at multiple stages, they often occur at greater frequency in younger stages. Other models of star-forming tidal debris often indicate that strong bursts of star formation occur early in interactions, soon after periaapse (Chien 2010; Di Matteo et al. 2008, Mihos & Hernquist 1994). Perhaps as a consequence, M11 noted that

the most successfully star cluster-forming tails of their sample were all relatively young ( $\lesssim 250$  Myr), although they did not find a statistically significant difference in the age distributions of SCC-rich and SCC-poor tails.

In Figure 8 we exhibit normalized histograms of HI properties of identically sized pixels from young (<250 Myr; blue) and old ( $\geq 250$  Myr; orange) tails. Ages are from M11 and sources therein (see Table 1); the age cut was selected to approximate the median of the M11 age distribution ( $\approx 300$  Myr). For all examined properties, these two categories of tails are typically quite different; younger tails enjoy higher column densities, have less gas with high velocity gradients ( $\gtrsim 15$  km s<sup>-1</sup> kpc<sup>-1</sup>) over relatively large scales ( $\sim 10$  kpc), but have a wider range of local ( $\sim$ kpc-scale) velocity dispersions. There is more gas with  $\sigma_{\text{los}}$  measurements  $\gtrsim 20$  km s<sup>-1</sup>. The fractions of unfitted pixels for these HI characteristics tend also to be lower in younger tails ( $f_{\text{unfit}} \approx 0.06$ , compared to  $\approx 0.15$ – $0.23$  for older tails). Consequently, the HI of younger tails have higher mechanical energy densities on average. In all, the HI gas in younger tails may be under higher pressures and is more kinematically disturbed than that of older tails.

Figure 9 contrasts the contoured HI parameter space of young and old tails in the top and bottom rows, respectively, along with their SCC-carrying pixels. There are more probable SCCs in younger tails, despite the larger number of older tails in our sample (by a factor of  $\approx 2$ ). Their host pixels follow the higher percentage of higher column density and turbulent gas ( $\approx 52\%$  compared to 27%), as well as the higher percentage of high mechanical energy densities and low large-scale velocity gradients ( $\approx 86\%$  compared to 43%). As before, there are pixels with possible SCCs in low-N<sub>HI</sub> areas in tails of all ages; the fraction of these with unfitted HI characteristics is higher in older tails than in younger tails.

Debris like NGC 1614N/S are examples of older tidal regions with ongoing or prolonged star cluster formation, broadening the distributions of HI properties of older tails and contributing high-probability cluster-carrying pixels in the bottom plots of Figure 9. The unplotted tail NGC 6872W shows most of the black points in the “subcritical” regions of the left plot of its contour diagram in the Online Figure Set 5, perhaps as a consequence of



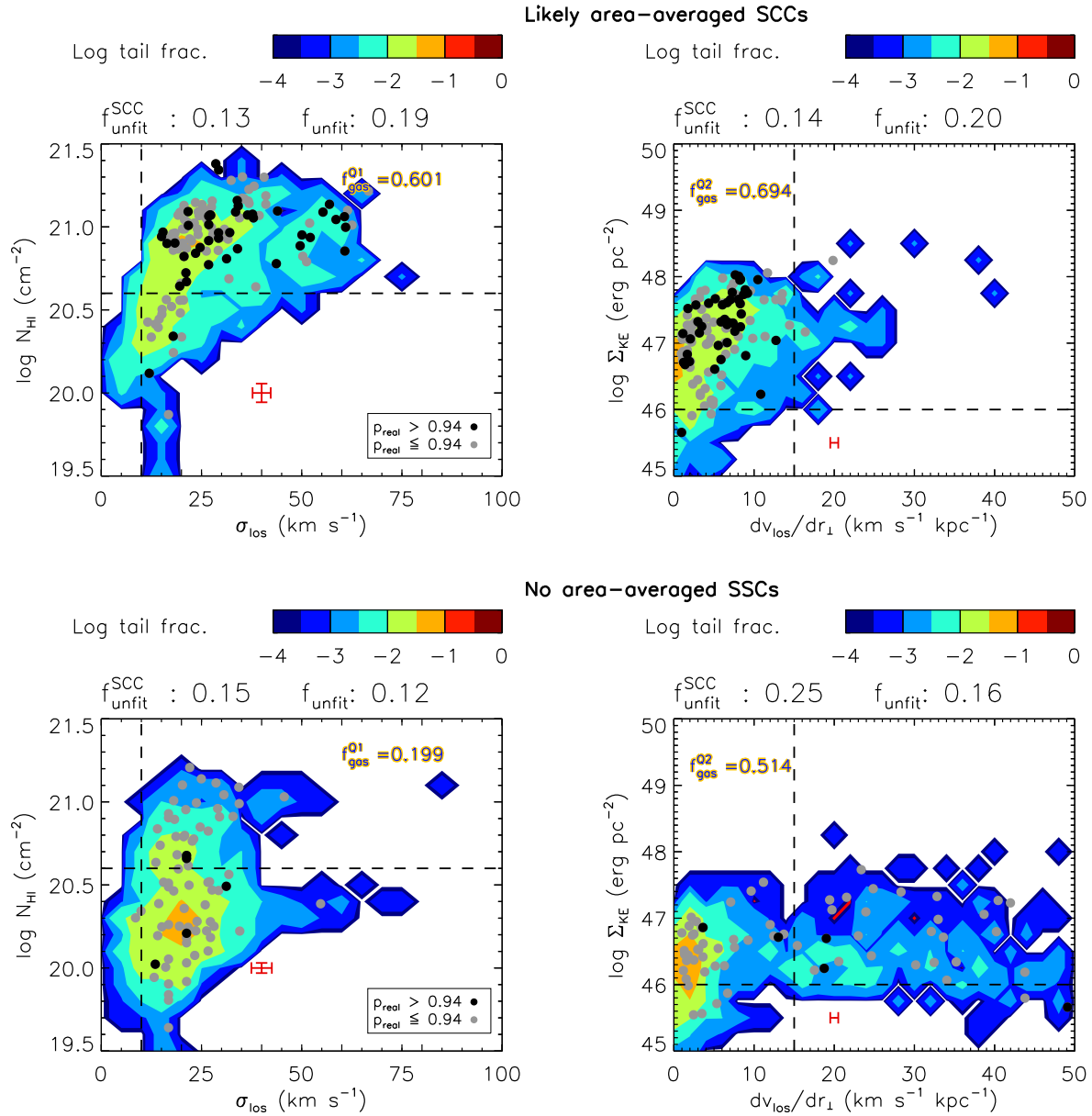


Fig. 7.— Combined, contoured distribution of measured H I quantities for tails with widespread SCC populations (M11; top row), and those without (bottom row) with levels corresponding to the fraction of the tail subsample within the indicated parameter space. Pixels with SCCs most likely to have star clusters are plotted in black ( $p_{\text{real}} > 0.94$ ), and those less likely in gray ( $p_{\text{real}} < 0.94$ ). The fraction of unfitted pixels, and the sample fraction within the specified quadrants Q1 (left) and Q2 (right) are provided. These are defined by the intersection of lines of potential threshold column density (Maybate et al. 2007) with the thermal-turbulent velocity dispersion in the first plots; and their combined energy density with the value of shear in the solar neighborhood in the right plots. See §5.1.1 for details.

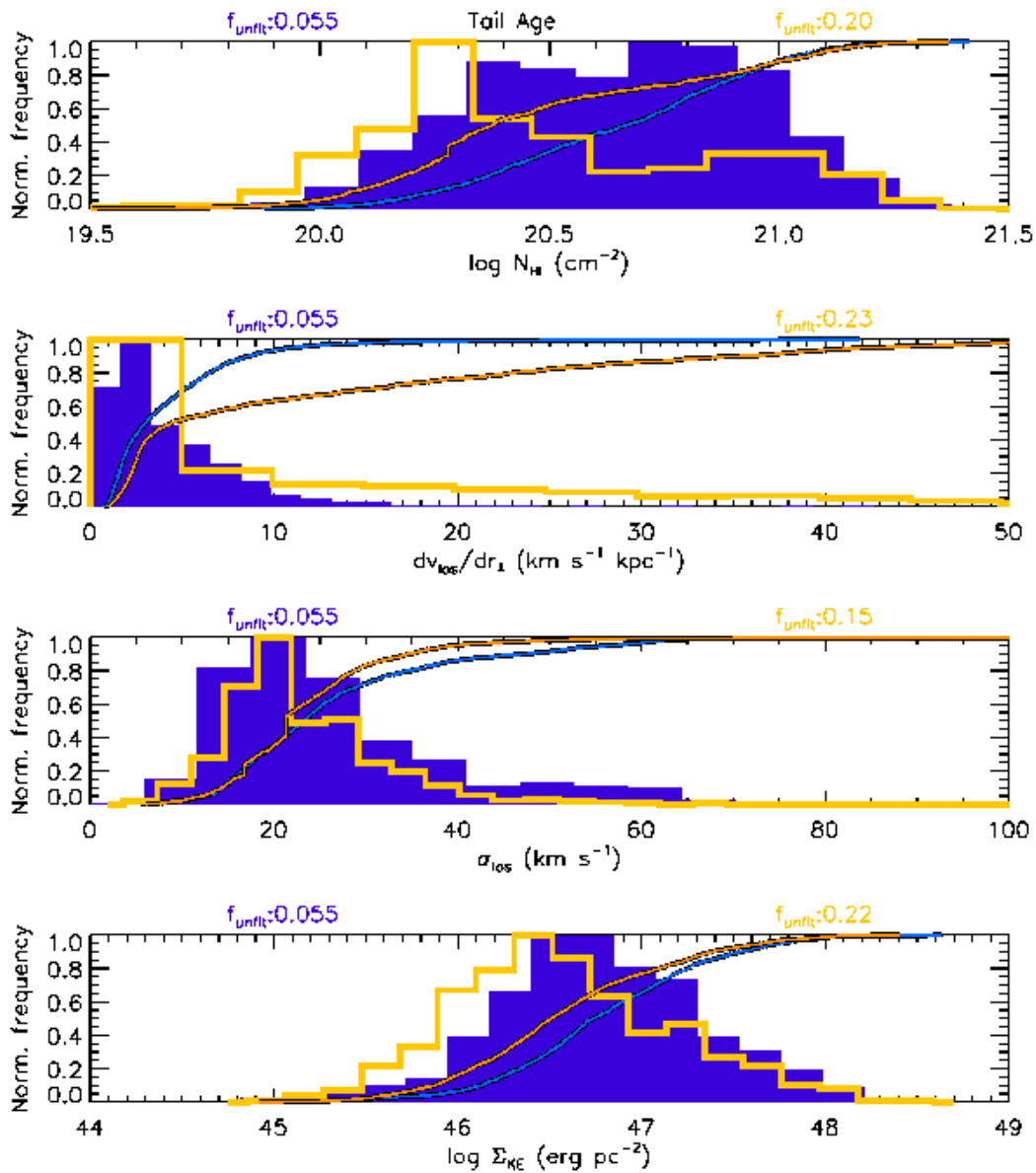


Fig. 8.— Normalized histograms of  $N_{\text{HI}}$ ,  $dv_{\text{los}}/dr_{\perp}$ ,  $\sigma_{\text{los}}$ , and  $\Sigma_{\text{KE}}$  for identically-sized pixels from young ( $<250$  Myr; blue) and old ( $\geq 250$  Myr; orange) tail regions in our sample. The fraction of unfitted pixels  $f_{\text{unfit}}$  is also recorded (see §5.1.2 for details). A full resolution version of this figure is available in *The Astrophysical Journal*.

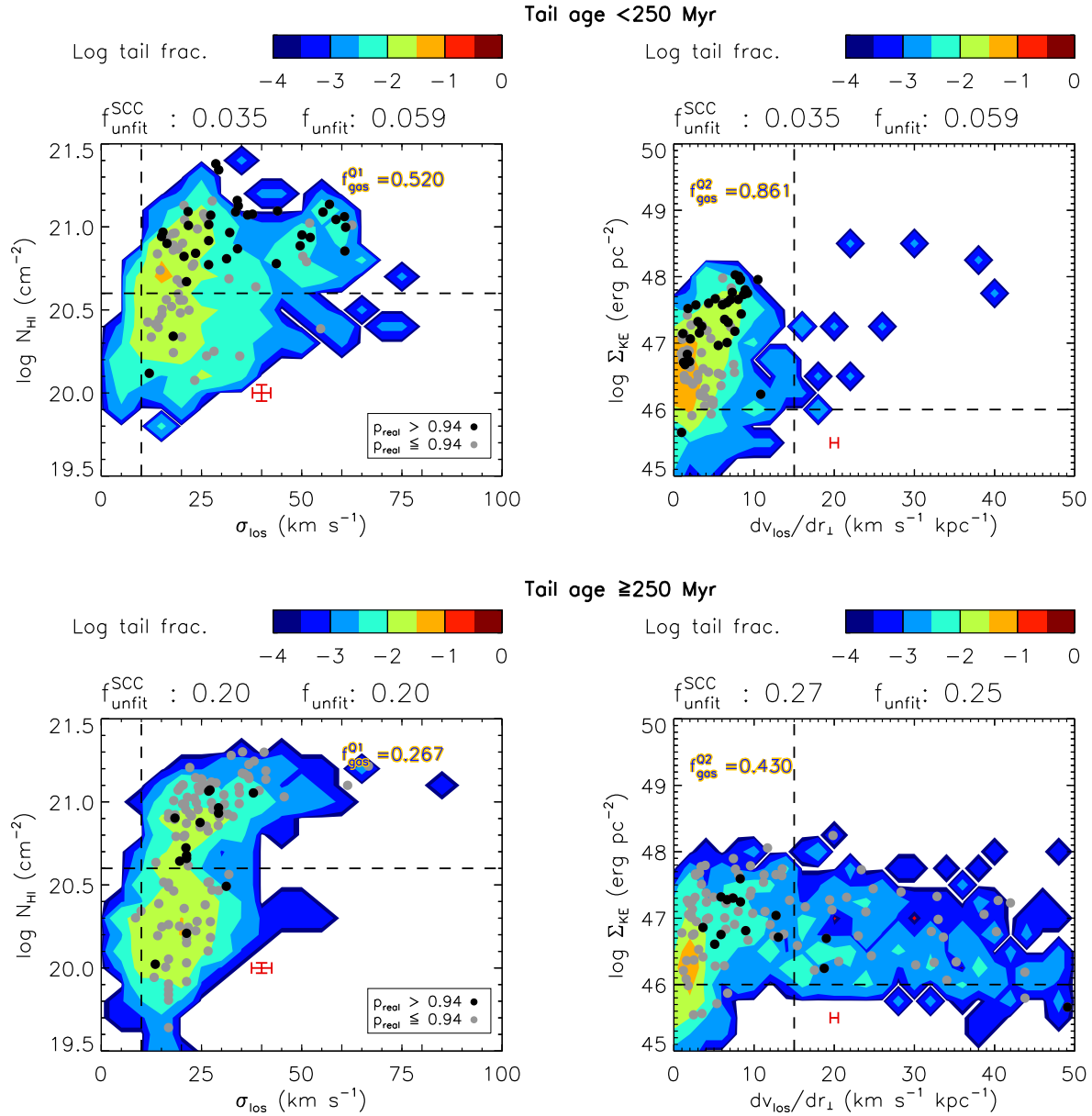


Fig. 9.— Combined, contoured distribution of measured HI quantities for young (<250 Myr) tails (top row), and old ( $\geq 250$  Myr) tails (bottom row), with levels corresponding to the fraction of the tail subsample within the indicated parameter space. Pixels with SCCs most likely to have star clusters are plotted in black ( $p_{\text{real}} > 0.94$ ), and those less likely in gray ( $p_{\text{real}} < 0.94$ ). The fraction of unfitted pixels, and the sample fraction within the specified quadrants Q1 (left) and Q2 (right) are provided. These are defined by the intersection of lines of potential threshold column density (Maybhatte et al. 2007) with the thermal-turbulent velocity dispersion in the left plots; and their combined energy density with the value of shear in the solar neighborhood in the right plots. See §5.1.2 for details.

its large beam size (diluting smaller-scale  $N_{\text{HI}}$  concentrations) or rapid HI depletion. Both of these cases are described in the Appendix. But in general these results are consistent with findings in the literature reporting the significance of young ages in establishing the necessary conditions—ambient densities and pressures—for star forming behavior.

Shearing kinematics in tidal debris also help explain the dispersion of SCC positions in especially older tails. Given the witnessed velocity gradients of galactic disks and debris regions examined here ( $\approx 0\text{--}20 \text{ km s}^{-1} \text{ kpc}^{-1}$  on average), it is likely that star clusters migrate a significant distance from their “original” HI pixels by the time they are observed. An order-of-magnitude estimate reveals that clusters can move several pixels (several kpc) away from their original pixel by the cutoff age of 250 Myr for these plots. Combined with age-dependent HI depletion and the tendency of clusters to fade as their stellar populations evolve (e.g., M11 and references therein), a tighter correlation between SCC detections and HI column densities and kinematics should logically be expected for young tails than older tails.

### 5.1.3. HI and Progenitor Mass Ratio

Major mergers outnumber minor mergers in our sample by a factor of  $\approx 2$ . The normalized histograms of Figure 10 show that tails from minor mergers seem to have a larger fraction of relatively high column density HI than do tails from major mergers. Most of their gas, however, has line-of-sight velocity dispersions  $< 40 \text{ km s}^{-1}$ , while major mergers have a slightly more extended distribution of  $\sigma_{\text{los}}$  out to  $\approx 50 \text{ km s}^{-1}$ . The overall appearance of the  $\sigma_{\text{los}}$  histograms for these two types of tails is somewhat similar, but appears statistically independent. Given the higher fraction of HI with column densities  $\gtrsim 10^{20.6} \text{ cm}^{-2}$  in our subsample of tails from minor encounters, this tail type also enjoys a bump in kinetic energy density histogram towards  $\log \Sigma_{\text{KE}} \gtrsim 46.5\text{--}47 \text{ erg pc}^{-2}$ .

The distributions of  $dv_{\text{los}}/dr_{\perp}$  are the most strikingly different between tails from major and minor encounters. Velocity gradients appear largely confined to values below  $\approx 10 \text{ km s}^{-1} \text{ kpc}^{-1}$  on  $\approx 10 \text{ kpc}$  scales for the latter category, while our set of tails from major mergers has a drastically broader range of  $dv_{\text{los}}/dr_{\perp}$  values.

Furthermore, tails from major mergers have a consistently higher fraction of unfitted pixels ( $\approx 20\%$ ) than tails from minor mergers ( $\approx 2\%$ ).

Many of these trends are of course reflected in the associated contoured distributions of these two types of tails in Figure 11, with the addition of SCC-carrying pixels as before. There are clearly more cluster candidates of both relatively high and low probability in the tails of major interactions than in minor ones, but again tails from major interactions outnumber those from minor interactions 14 to 6 in this figure. Despite much of the HI gas inhabiting the ostensibly subcritical column density region of the parameter space explored in the top row (major encounters) of Figure 11, many of the pixels with high probabilities of having at least one cluster still lie in the higher column density region.

Between the evident trend of minor merger tails having higher  $N_{\text{HI}}$  overall and/or a smaller range of  $dv_{\text{los}}/dr_{\perp}$  for this medium, it is possible that major mergers are prone to more intense interactions. A higher HI dispersal efficiency may be possible in major interactions; the larger fractions of unfitted pixels in tails from these encounters might testify to this. Stronger interactions may also engender greater disruptions to the velocity fields on  $\sim 10 \text{ kpc}$  scales. For example, Keel & Borne (2003) find that the major merger NGC 6621/2 exhibits strong H $\alpha$  velocity perturbations and has an extensive population of star clusters. This contrasts with their observations of NGC 5752/4, a minor merger with evidently less kinematic disruption. While the interaction ages of these two collisions are different ( $\sim 100 \text{ Myr}$  for the former and  $\sim 250 \text{ Myr}$  for the latter), Keel & Borne contend that star cluster formation depends on a mass ratio-modulated strength of the interaction more than the interaction stage. However, they also examine cluster populations across the progenitor galaxy disks rather than just the tidal debris, making these studies difficult to compare.

But most critically, it must be noted that the single and combined distributions of HI properties of tail pixels from minor and major mergers bear a qualitative resemblance to those from young and old tails, respectively. This can be seen by comparing Figure 9 with Figure 11. Table 1 shows that this results from the limited sample size; while the M11 sample is reasonably mixed in terms of

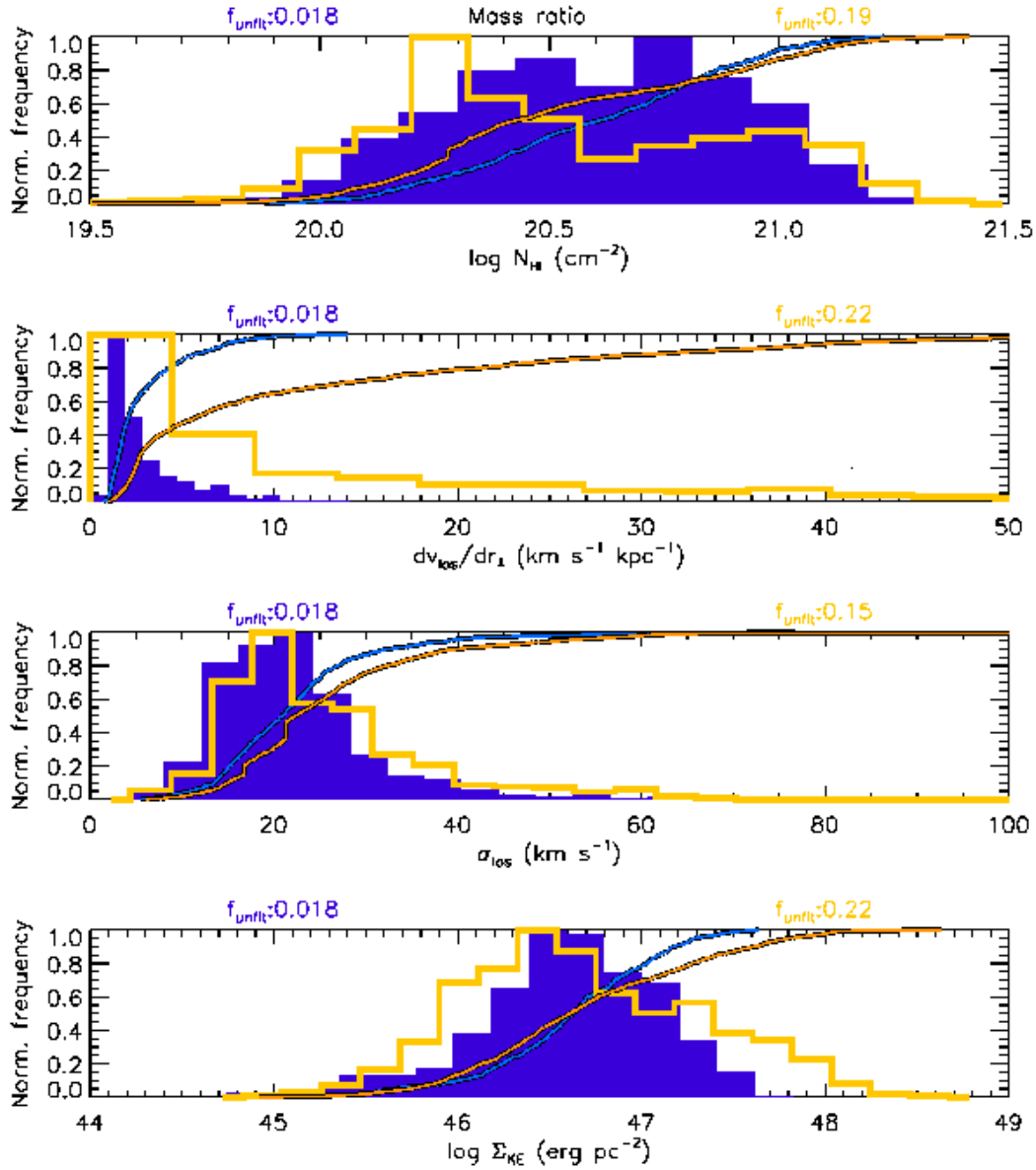


Fig. 10.— Normalized histograms of  $N_{\text{HI}}$ ,  $dv_{\text{los}}/dr_{\perp}$ ,  $\sigma_{\text{los}}$ , and  $\Sigma_{\text{KE}}$  for identically-sized pixels from tails from minor ( $M_2/M_1 < 1$ ; blue) and major ( $M_2/M_1 \geq 1$ ; orange) encounters in our sample. The fraction of unfitted pixels  $f_{\text{unfit}}$  is also recorded (see §5.1.3 for details). A full resolution version of this figure is available in *The Astrophysical Journal*.

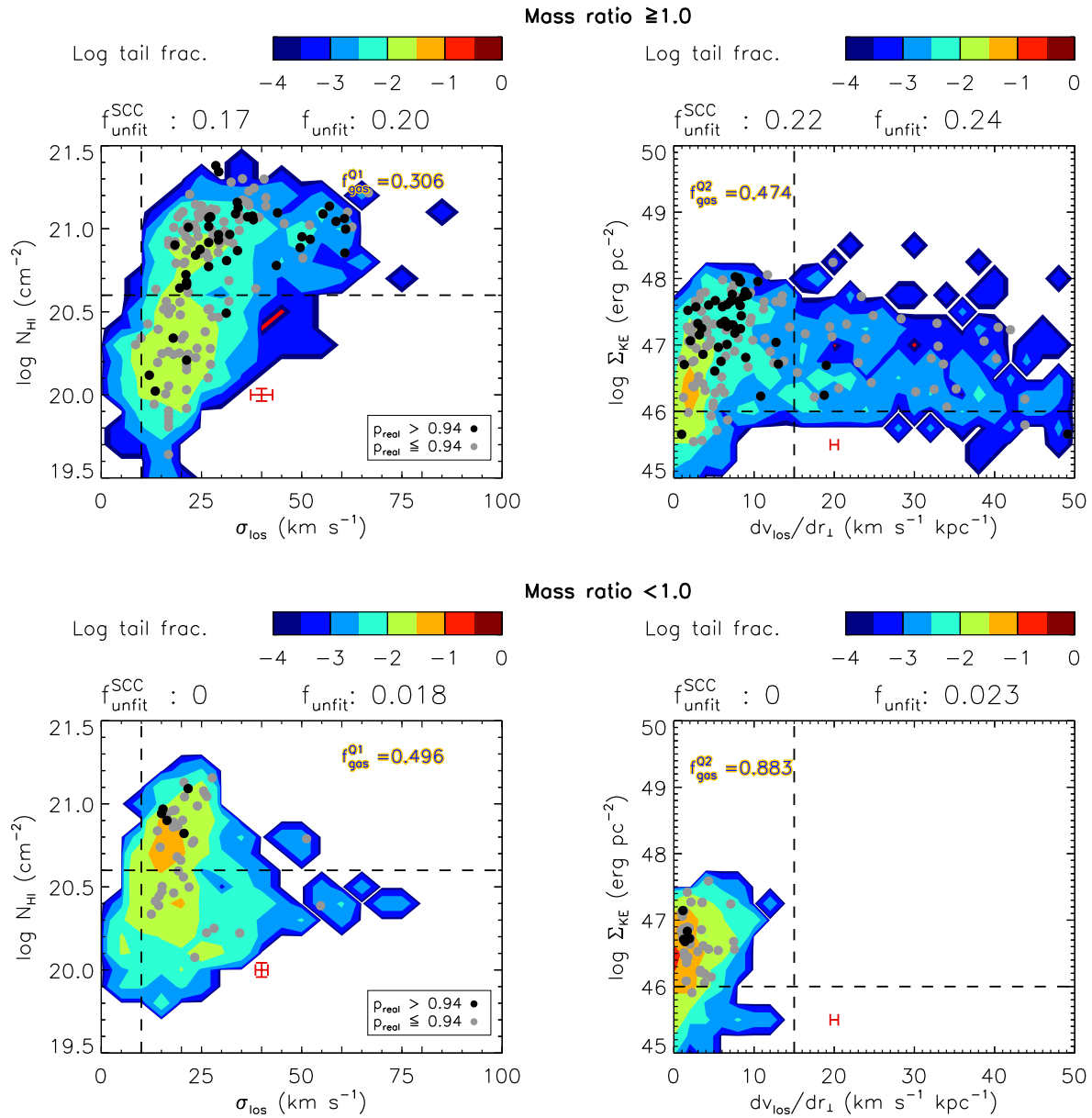


Fig. 11.— Combined, contoured distribution of measured HI quantities for tails from major ( $M_2/M_1 \geq 1$ ; top row) and minor ( $M_2/M_1 < 1$ ; bottom row) encounters, with levels corresponding to the fraction of the tail subsample within the indicated parameter space. Pixels with SCCs most likely to have star clusters are plotted in black ( $p_{\text{real}} > 0.94$ ), and those less likely in gray ( $p_{\text{real}} < 0.94$ ). The fraction of unfitted pixels, and the sample fraction within the specified quadrants Q1 (left) and Q2 (right) are provided. These are defined by the intersection of lines of potential threshold column density (Maybhatte et al. 2007) with the thermal-turbulent velocity dispersion in the left plots; and their combined energy density with the value of shear in the solar neighborhood in the right plots. See §5.1.3 for details.

age and mass ratio, the subsample attributed to Knierman et al. (2003) supplies a large number of older tails from major encounters. Thus, while our observations and analyses can be viewed through the lens of interaction age and/or mass ratio, our finite sample size makes it difficult to ascertain the effects of one or the other. Removing the Knierman et al. (2003) sample for this work would only further decrease the sample size and make any results more sensitive to particular tails and their unstudied additional effects that certainly contribute to their SCC populations. We therefore opt not to do that here. Rather, we maintain that a *combination* of tail age and progenitor mass ratio (and likely a number of other variables not studied here) is at least partly responsible for the HI and SCC phenomenology we present.

## 5.2. Turbulence: A Cause or Consequence of Star Formation?

Supernovae (SNe), particularly Type II, are generally regarded as the dominant source of feedback in the ISM in galactic contexts (e.g., van den Bosch 2000; Tasker & Bryan 2008; Tasker & Bryan 2006; Spitzer 1990). It then becomes a question for this project of whether the supernovae produced in prior star formation events are the primary source of the mechanical energies observed in the neutral HI in these tidal tails. That is, do the kinetic energy densities (and presumably pressures) we measure result from star and cluster formation, or are they the cause of star and cluster formation?

Using UV/IR-derived star formation rates (SFRs) of a sample of relatively low inclination disk galaxies in the THINGS survey, Tamburro et al. (2009) calculated the pixel-by-pixel kinetic energy densities that would be produced from feedback from core-collapse SNe. In comparing these to measurements of the actual HI energy densities, they find that the efficiency of energy injection from SNe would have to be unrealistically high in order for their measured  $\Sigma_{\text{KE}}$  values to be supplied by star formation. Not having a uniform survey of UV, IR, or H $\alpha$  diagnostics of star formation rates for our sample, we instead aim to determine the potential star formation rates of our tidal tails from their  $\Sigma_{\text{KE}}$  and suggest whether the results are reasonable for this kind of environment.

As in Tamburro et al. (2009), we begin by equating the kinetic energy density to that theoretically provided by supernovae; i.e.  $\Sigma_{\text{KE}} = \epsilon_{\text{SN}} \dot{E}_{\text{SN}} \tau_{\text{SN}}$ .  $\dot{E}_{\text{SN}}$  is the rate at which energy is released by SNe, which is a function of the SFR;  $\epsilon_{\text{SN}}$  is the efficiency with which that energy is converted to the observed turbulence, and  $\tau_{\text{SN}}$  is the turbulence dissipation rate. Combining their Equations (5)–(7), characterizing the dissipation timescale and fraction of the stellar populations that produce SNe, we derive the following expression for the pixel-by-pixel SFR ( $\Upsilon$ ):

$$\begin{aligned} \frac{\Upsilon}{M_{\odot} \text{ yr}^{-1}} &= 2.03 \times 10^{-3} \frac{\alpha}{\epsilon_{\text{SN}}(1 + f_{1a})} \\ &\times \left( \frac{f_{\text{SN}}}{\langle M/M_{\odot} \rangle} \right) \left( \frac{\lambda}{100 \text{ pc}} \right)^{-1} \\ &\times \left( \frac{M_{\text{HI}}}{M_{\odot}} \right) \left( \frac{\sigma_{\text{los}}}{10 \text{ km s}^{-1}} \right)^3. \quad (9) \end{aligned}$$

As before,  $\alpha$  corresponds to the degree of isotropy (here assumed to be 3/2), and the factor  $1/(1+f_{1a})$  is a term included in our derivation to account for the fractional contribution of type-1a SNe. Following Mannucci et al. (2005), we consider  $f_{1a}$  values in the range 0–0.33. The term  $f_{\text{SN}}$  indicates the fraction of (recently formed) stars that end as core-collapse SNe, while  $\langle M/M_{\odot} \rangle$  denotes the average mass of the stellar population within the examined region. Dividing these two terms in the equation, we consider values in the range  $0.9 \times 10^{-2}$  to  $1.3 \times 10^{-2}$ , as shown by Tamburro et al. (2009) for an upper IMF mass limit of 20–50  $M_{\odot}$ , with a mass function of the form  $\phi(m) = m^{-\alpha_0}$ ;  $\alpha_0 = 1.3$  for 0.1–0.5  $M_{\odot}$  and 2.3 for 0.5–120  $M_{\odot}$  (e.g., Calzetti et al. 2007 and references therein). We use values in the range 0.1–0.5 for the efficiency  $\epsilon_{\text{SN}}$ ; the lower limit is suggested by numerical simulations (Thornton et al. 1998), and the upper limit provides a conservative lower limit to  $\Upsilon$ . The turbulence driving scale is given by  $\lambda$ , which simulations predict to be  $100 \pm 30$  pc (Joung & Mac Low 2006; de Avillez & Breitschwerdt 2007). The mass of HI is  $M_{\text{HI}}$ , and  $\sigma_{\text{los}}$  as defined here. Note the additional factor of  $\sigma_{\text{los}}$ ; this results from the implicit expression of  $\tau_{\text{SN}}$  in terms of  $\lambda$  and  $\sigma_{\text{los}}$ . The constant  $2.03 \times 10^{-3}$  incorporates all unit conversions and the  $10^{51}$  erg that are assumed to be released from each type II SN event (Heiles 1987).

**Table 5.**  
Hypothetical Star Formation Rates

Tail	Variable Pix. Scale		Const. Pix. Scale	
	min. $\Upsilon$ ( $M_{\odot}$ $\text{yr}^{-1}$ )	max. $\Upsilon$ ( $M_{\odot}$ $\text{yr}^{-1}$ )	min. $\Upsilon$ ( $M_{\odot}$ $\text{yr}^{-1}$ )	max. $\Upsilon$ ( $M_{\odot}$ $\text{yr}^{-1}$ )
NGC 1487E	0.056	1.0	0.15	2.7
NGC 1487W	0.035	0.62	0.069	1.2
NGC 4747	0.0079	0.14	0.0053	0.095
NGC 520	0.080	1.4	0.080	1.4
NGC 2992	9.1	160	11.	190
NGC 2993	3.0	53.	2.8	50.
NGC 2782E	2.6	47.	3.1	56.
NGC 2782W	0.53	9.4	0.54	9.7
NGC 2444	1.1	20.	1.3	23.
NGC 2535	1.5	28.	1.9	33.
NGC 6872E	18.	320	18.	320
NGC 6872W	15.	260	14.	260
NGC 1614N	0.44	7.9	0.48	8.6
NGC 1614S	0.24	4.3	0.48	8.6
NGC 4038A	0.022	0.39	0.0082	0.15
NGC 4038B	0.0011	0.020	0.0019	0.033
NGC 4038C	2.2e-4	0.0039	2.4e-4	0.0042
NGC 3256E	2.3	41.	3.2	57.
NGC 3256W	6.0	110	7.4	130
NGC 7252E	0.26	4.6	0.26	4.6
NGC 7252W	2.4	43.	2.9	52.
NGC 3921S	1.5	26.	1.5	26.

We then mapped out the pixel-by-pixel SFR of all the tails using our maps of  $\Sigma_{M_{\text{HI}}}$  and  $\sigma_{\text{los}}$ , for the combinations of aforementioned constants that yield the smallest and greatest result. We performed this for both original maps and those produced at the constant pixel scale. In practice, changing the efficiency of injection  $\epsilon_{\text{SN}}$  has the dominant affect in this equation; we added the results of all pixels belonging to individual tails and record the results in Table 5. We posit that if the tail-wide ongoing star formation rate (of similar timescale as the turbulence dissipation timescale) could fall between the ranges quoted in this table, it is possible that star formation and the SNe explosions that result from it generally caused the turbulent kinetic energy densities we observe rather than was an effect of it. Ideally, uniformly deep, wide-field imaging in  $\text{H}\alpha$  of our tail sample would provide the star formation rate on the corresponding timescale ( $\sim 10$  Myr), allowing a direct and straightforward comparison. Unfortunately, no such survey exists.

There are a few potentially elucidating case studies, however. Knierman et al. (2012) find a  $\text{H}\alpha$ -derived SFR for the entire western tail of NGC 2782 of  $9 \times 10^{-6} M_{\odot} \text{yr}^{-1} \text{kpc}^{-2}$ . Adjusting for the in-tail area used here, we calculate a rate  $\Upsilon \approx 2 \times 10^{-3} M_{\odot} \text{yr}^{-1}$ . This is several orders of magnitude lower than the values reported

in Table 5; thus the  $\text{H}\text{I}$  turbulence is not likely caused by star formation in this case. Moreover, the  $\text{H}\alpha$  data of Mihos et al. (1993) indicate that most current star formation in NGC 6872 is confined to its tidal tails, and is occurring at a rate  $\sim 3 M_{\odot} \text{yr}^{-1}$ . The individual rates for the eastern and western tails must be smaller; but in either case the rate is far below the minimum  $\Upsilon$  needed ( $\sim 15 M_{\odot} \text{yr}^{-1}$  for either tail and pixel size) for the observed turbulent energy to be supplied by feedback from star formation overall.

While the turbulence we observe is purely on  $\sim \text{kpc}$  scales, it is likely crucial to the kinematic nature of the ISM on smaller, star-forming ( $\sim \text{pc}$ ) scales. Turbulence is injected on hundreds of pc to  $\sim \text{kpc}$ -scales (e.g., Mac Low 1999; Elmegreen 1993; Block et al. 2010), and cascades down to smaller scales until it is dissipated into thermal energy by viscosity (Elmegreen et al. 2003; Kolmogorov 1941). There are a number of observed radiative pathways available to eliminate this energy effectively and faster than the turbulence decay timescale by several orders of magnitude; e.g., collisionally-excited lines of  $\text{C}\text{IV}$  (Wolfire et al. 2003), rovibrational transitions of  $\text{H}_2$  (eg. Cluver et al. 2010), and radio/X-ray continuum emission (Kaufman et al. 2012).

In effect, we are left with a top-down evolutionary process, where gas kinematics at observably large scales—likely influenced by a combination of tail age and progenitor mass ratio as seen in Section 5.1—influences star formation on the otherwise unresolved, smaller scales. Turbulent gas generates a log-normal density probability density function (PDF) in the local ISM (Wada et al. 2002), whose width—dispersion in density—increases mainly with turbulent Mach number (Krumholz & Thompson 2007). Thus, turbulence on large scales affects the density distribution of gas on small scales. This is exacerbated in mergers, where additional, expeditious kinematic perturbations create deviations in the log-normal distribution, favoring more high-density gas (Bournaud 2011).

In all, our results present a compelling case for the importance of interaction-established, kpc-scale  $\text{H}\text{I}$  kinematics and column densities in determining the capacity of pc-scale star cluster formation in tidal debris. Other, currently unsurveyed interaction properties—e.g., dark matter halo po-



tentials, interaction speeds and impact parameters, H<sub>2</sub> content, and dust-to-gas ratios—may help set the stage for luminous star cluster formation in tidal tails and may help account for the variety and distribution of SCC populations witnessed here. However, the character of the neutral hydrogen medium, described by its densities, pressures, and kinematics, also appears to be an invaluable factor in this process. We have shown that high-confidence SCC detection often occurs in tails with large fractions of high column density, turbulent gas (Section 5.1.1). Both the putative star cluster populations and the underlying HI medium clearly varies depending on the age (Section 5.1.2) and/or the progenitor galaxy mass ratio (Section 5.1.3 ) of the interaction, indicating that these dynamical properties are important in tidal tail star cluster formation as well.

## 6. Conclusions

In this paper, we have performed a pixel-by-pixel characterization and analysis of the HI content of 22 tidal debris fields from pairwise galaxy interactions, comparing these properties between pixels that contain star cluster candidates (SCCs) and those that do not. In our tail sample we measured HI column density  $N_{\text{HI}}$ , mass density  $\Sigma_{M_{\text{HI}}}$ , line-of-sight velocities  $v_{\text{los}}$  and velocity dispersions  $\sigma_{\text{los}}$ , as well as mechanical energy densities  $\Sigma_{\text{KE}}$  to the best pixel-scale spatial resolutions ( $\sim$ kpc) our archival data afford. We also constructed a tracer of the locally-centered line-of-sight velocity gradient  $dv_{\text{los}}/dr_{\perp}$  for these regions, examining the velocity fields of the tails over larger,  $\sim$ 10 kpc scales.

While tail gas kinematics and geometry, small-scale star and cluster formation events, and feedback likely produce dispersion in our results, it appears that many “successful” kpc-scale triggered clustered star formation events often take place in  $\sim$ kpc-scale regions of high HI gas column and kinetic energy densities. Kinetic energy density should generally trace HI pressures (integrated along the line of sight), so this would imply that clustered star formation as detected by M11 requires high pressures (high  $\Sigma_{\text{KE}}$  from moderately turbulent gas), but also high  $N_{\text{HI}}$  on these scales. It is possible that these conditions could arise from intermittent, compressive tides (e.g.,

Renaud et al. 2009) or gravitational instabilities (e.g., Bournaud 2010).

We repeated our analysis for data regridded to a constant pixel scale, and compared the distributions of HI properties between tails of different global cluster populations, dynamical ages, and progenitor mass ratios. Despite variation in individual tail phenomenology and SCC populations, several clear trends and contrasts are evident in the HI content of these types of tails:

1. Tails with global cluster populations (as identified in M11) tend to have HI gas of higher column and kinetic energy densities than tails with no apparent tail-wide cluster populations, with much of it ( $\gtrsim$ 50%) above the putative  $\log N_{\text{HI}} = 20.6 \text{ cm}^{-2}$ ,  $\log \Sigma_{\text{KE}} = 46 \text{ erg pc}^{-2}$  thresholds mentioned here. The distribution of velocity dispersions also has a greater contribution of high values ( $\sigma_{\text{los}} \gtrsim 30 \text{ km s}^{-1}$ ).
2. Relatively young tails (dynamical age  $< 250$  Myr) have more pixels with high probability clusters than older tails ( $\geq 250$  Myr), and contain gas with larger column and kinetic energy densities on average. There is also more gas overall at high velocity dispersions ( $\sigma_{\text{los}} \gtrsim 30 \text{ km s}^{-1}$ ) in these types of tails. Older tails are more likely to be affected by age-dependent fading in their cluster populations as well.
3. Tails from minor encounters appear to have more relatively high column density HI than tails from major interactions. When measured over a common,  $\sim$ 10 kpc-scale velocity field, major encounters appear typically slightly more capable of driving the gas to higher ( $> 10 \text{ km s}^{-1} \text{ kpc}^{-1}$ ) velocity gradients. The strength of the encounter, gauged in part by the interacting mass ratio (among other variables) may help control the efficiency of HI dispersal and disruption of the velocity fields in its resulting tidal debris. Major mergers may drive gas to high kpc-scale velocity dispersions, but may also encourage stronger local depletion and larger-scale shearing motions in certain cases.
4. Because of the strong degeneracy in our sample between old tails and tails from major

interactions, it cannot be well determined whether the observations noted above are explained by primarily age or mass ratio, or a combination of the two. Other unstudied properties like interaction speed, dark matter halo structure, and ISM dust-to-gas ratios are likely to also play roles in star cluster formation in tidal tails.

5. In calculating the required star formation rate (SFR) for the turbulent energies to be provided by feedback from star formation, we deduce that it is unlikely that the kinetic energy densities of the HI medium are a consequence of star formation, but rather a pre-existing environmental condition. However, we can only verify this for a few systems that have data of SFR indicators (i.e.  $H\alpha$ ) that trace activity around the same timeframe as the  $\sim 10$  Myr turbulence injection and dissipation.

While these results are promising, much work remains in resolving certain issues. Additional optical photometry (e.g., broadband  $UB$  coverage to add to existing  $VI$  images) is required to accurately age-date cluster candidates for a more precise comparison to HI properties than the probabilistic work incorporated here. A larger tail sample would also allow a more robust comparison between HI measurements between certain tail types, and additional subcategories within. A homogeneous  $H\alpha$  survey of the tidal debris sample would facilitate a quantitative comparison between hypothetical star formation rates calculated here, and their measured equivalents over the appropriate  $\approx 10$  Myr timescale. Lastly, consistent modeling of all interacting systems would provide a direct link from the projected quantities we observe here to real physical properties like HI number density and local pressure.

We thank the anonymous referee for helpful comments and suggestions that greatly improved the clarity and results of this paper. This project was supported by a grant from the Space Telescope Science Institute (grant no. HST-GO-11134.05-A). Funding was also provided by the National Science Foundation under award AST-0908984. The Institute for Gravitation and the

Cosmos is supported by the Eberly College of Science and the Office of the Senior Vice President for Research at the Pennsylvania State University.

*Facilities:* VLA, ATCA, WSRT

## REFERENCES

- Ajhar, E. A., Blakeslee, J. P., & Tonry, J. L. 1994, *AJ*, 108, 2087
- Alonso-Herrero, A., Engelbracht, C. W., Rieke, M. J., Rieke, G. H., & Quillen, A. C. 2001, *ApJ*, 546, 952
- Anders, P., Lamers, H. J. G. L. M., & Baumgardt, H. 2009, *A&A*, 502, 817
- Appleton, P. N., Ghigo, F. D., van Gorkom, J. H., Schombert, J. M., & Struck-Marcell, C. 1987, *Nature*, 330, 140
- Bastian, N., Hempel, M., Kissler-Patig, M., Homeier, N.L., & Trancho, G. 2005, *A&A*, 435, 65
- Bastian, N., & Gieles, M. 2008, *Mass Loss from Stars and the Evolution of Stellar Clusters*, 388, 353
- Bigiel, F., Leroy, A., Walter, F., Blitz, L., Brinks, E., de Blok, W. J. G., & Madore, B. 2010, *AJ*, 140, 1194
- Block, D. L., Puerari, I., Elmegreen, B. G., & Bournaud, F. 2010, *ApJ*, 718, L1
- Blitz, L., & Rosolowsky, E. 2004, *ApJ*, 612, L29
- Blitz, L., & Rosolowsky, E. 2006, *ApJ*, 650, 933
- Bournaud, F. 2010, *Galaxy Wars: Stellar Populations and Star Formation in Interacting Galaxies*, 423, 177
- Bournaud, F., Duc, P.-A., Amram, P., Combes, F., & Gach, J.-L. 2004, *A&A*, 425, 813
- Bournaud, F. 2011, *EAS Publications Series*, 51, 107
- Braine, J., Duc, P.-A., Lisenfeld, U., Charmandaris, V., Vallejo, O., Leon, S., & Brinks, E. 2001, *A&A*, 378, 51
- Briggs, D. S., Schwab, F. R., & Sramek, R. A. 1999, *Synthesis Imaging in Radio Astronomy II*, 180, 127
- Brinks, E., Duc, P.-A., & Walter, F. 2004, *Recycling Intergalactic and Interstellar Matter*, 217, 532

- Calzetti, D., Kennicutt, R. C., Engelbracht, C. W., et al. 2007, *ApJ*, 666, 870
- Casasola, V., Bettoni, D., & Galletta, G. 2004, *A&A*, 422, 941
- Chien, L. 2010, *Astronomical Society of the Pacific Conference Series*, 423, 197
- Cluver, M. E., Appleton, P. N., Boulanger, F., et al. 2010, *ApJ*, 710, 248
- de Avillez, M. A., & Breitschwerdt, D. 2007, *ApJ*, 665, L35
- de Grijs, R. 2010, *Royal Society of London Philosophical Transactions Series A*, 368, 693
- de Grijs, R., Lee, J. T., Mora Herrera, M. C., Fritze-v. Alvensleben, U., & Anders, P. 2002, *New Astronomy*, 8, 155
- Di Matteo, P., Bournaud, F., Martig, M., Combes, F., Melchior, A.-L., & Semelin, B. 2008, *A&A*, 492, 31
- Duc, P.-A., Brinks, E., Springel, V., Pichardo, B., Weilbacher, P., & Mirabel, I.F. 2000, *AJ*, 120, 1238
- Duc, P.-A., Bournaud, F., & Masset, F. 2004, *A&A*, 427, 803
- Efremov, I. N., & Ivanov, G. R. 1987, *Ap&SS*, 129, 39
- Elmegreen, B. G. 1993, *ApJ*, 411, 170
- Elmegreen, B. G. 2008, *ApJ*, 672, 1006
- Elmegreen, B. G., & Efremov, Y. N. 1997, *ApJ*, 480, 235
- Elmegreen, B. G., Elmegreen, D. M., & Leitner, S. N. 2003, *ApJ*, 590, 271
- English, J., & Freeman, K. C. 2001, *Gas and Galaxy Evolution*, 240, 858
- English, J., Norris, R. P., Freeman, K. C., & Booth, R. S. 2003, *AJ*, 125, 1134
- Getts, T. J. 2001. PhD Thesis, University of Virginia.
- Gieles, M., & Bastian, N. 2008, *A&A*, 482, 165
- Gil de Paz, A., Madore, B. F., Boissier, S., et al. 2005, *ApJ*, 627, L29
- Girardi, L., et al. 2008, *PASP*, 120, 583
- Guillard, P., Boulanger, F., Pineau des Forêts, G., et al. 2012, *ApJ*, 749, 158
- Hancock, M., Smith, B. J., Struck, C., Giroux, M. L., Appleton, P. N., Charmandaris, V., & Reach, W. T. 2007, *AJ*, 133, 676
- Haynes, M. P. 1979, *AJ*, 84, 1830
- Heiles, C. 1987, *ApJ*, 315, 555
- Hibbard, J. E., Guhathakurta, P., van Gorkom, J. H., & Schweizer, F. 1994, *AJ*, 107, 67
- Hibbard, J. E., van der Hulst, J. M., Barnes, J. E., & Rich, R. M. 2001, *AJ*, 122, 2969
- Hibbard, J.E. & van Gorkom, J.H., 1996, *AJ*, 111,655
- Hibbard, J. E., Vacca, W. D., & Yun, M. S. 2000, *AJ*, 119, 1130
- Hibbard, J. E., & Yun, M. S. 1996, *Cold Gas at High Redshift*, 206, 47
- Holtzman, J. A., Burrows, C. J., Casertano, S., Hester, J. J., Trauger, J. T., Watson, A. M., & Worthey, G. 1995, *PASP*, 107, 1065
- Horellou, C., & Koribalski, B. 2003, *Ap&SS*, 284, 499
- Horellou, C. & Koribalski, B. 2007, *A&A*, 464, 155
- Joung, M. K. R., & Mac Low, M.-M. 2006, *ApJ*, 653, 1266
- Kaufman, M., Brinks, E., Elmegreen, D. M., Thomasson, M., Elmegreen, B. G., Struck, C., & Klaric, M. 1997, *AJ*, 114, 2323
- Kaufman, M., Grupe, D., Elmegreen, B. G., et al. 2012, *AJ*, 144, 156
- Keel, W. C., & Borne, K. D. 2003, *AJ*, 126, 1257
- Kennicutt, R. C., Jr. 1989, *ApJ*, 344, 685
- Kennicutt, R. C., Jr. 1998, *ApJ*, 498, 541
- Knierman, K. 2007, *Island Universes - Structure and Evolution of Disk Galaxies*, 307
- Knierman, K.A., Hunsberger, S.D., Gallagher, S.C., Charlton, J.C., Whitmore, B., Kundu, A., Hibbard, J., & Zaritsky, D. 2003, *AJ*, 126, 1227
- Knierman, K., Knezek, P. M., Scowen, P., Jansen, R. A., & Wehner, E. 2012, *ApJ*, 749, L1
- Kolmogorov, A. 1941, *Akademiia Nauk SSSR Doklady*, 30, 301
- Konstantopoulos, I. S. 2010, *Galaxy Wars: Stellar Populations and Star Formation in Interacting Galaxies*, 423, 135

- Koopmann, R. A., et al. 2008, ApJ, 682, L85
- Krumholz, M. R., McKee, C. F., & Tumlinson, J. 2009, ApJ, 693, 216
- Krumholz, M. R., & Thompson, T. A. 2007, ApJ, 669, 289
- Kundu, A., & Whitmore, B. C. 2001, AJ, 121, 2950
- Larsen, S. S., & Richtler, T. 2000, A&A, 354, 836
- Lee, H. J., & Lee, M. G. 2005, Journal of Korean Astronomical Society, 38, 345
- Leroy, A. K., Walter, F., Brinks, E., et al. 2008, AJ, 136, 2782
- Liu, G., Koda, J., Calzetti, D., Fukuhara, M., & Momose, R. 2011, ApJ, 735, 63
- Mac Low, M.-M. 1999, ApJ, 524, 169
- Maíz Apellániz, J. 2009, ApJ, 699, 1938
- Mannucci, F., Della Valle, M., Panagia, N., et al. 2005, A&A, 433, 807
- Martinez-Badenes, V., Lisenfeld, U., Espada, D., et al. 2012, A&A, 540, A96
- Maybhate, A., Masiero, J., Hibbard, J. E., Charlton, J. C., Palma, C., Knierman, K. A., & English, J. 2007, MNRAS, 381, 59
- McKee, C. F., & Ostriker, J. P. 1977, ApJ, 218, 148
- Mihos, J. C., Bothun, G. D., & Richstone, D. O. 1993, ApJ, 418, 82
- Mihos, J. C., & Hernquist, L. 1994, ApJ, 431, L9
- Mullan, B., Konstantopoulos, I. S., Kepley, A. A., et al. 2011, ApJ, 731, 93
- Neff, S. G., et al. 2005, ApJ, 619, L91
- Neff, S. G., Hutchings, J. B., Standord, S. A., & Unger, S. W. 1990, AJ, 99, 1088
- Peterson, C. J. 1993, in *ASP Conf. Ser. 50, Structure and Dynamics of Globular Clusters*, ed. S. G. Djorgovsky & G. Meylan (San Francisco: ASP), 337
- Portegies Zwart, S. F., McMillan, S. L. W., & Gieles, M. 2010, ARA&A, 48, 431
- Renaud, F., Boily, C. M., Naab, T., & Theis, C. 2009, ApJ, 706, 67
- Robin, A. C., Reylé, C., Derrière, S., & Picaud, S. 2003, A&A, 409, 523
- Sault, R. J., Teuben, P. J., & Wright, M. C. H. 1995, *Astronomical Data Analysis Software and Systems IV*, 77, 433
- Saviane, I., Hibbard, J. E., & Rich, R. M. R. 2004, AJ, 127, 660
- Schweizer, F. 1978, in *IAU Symposium, Vol. 77, Structure and Properties of Nearby Galaxies*, ed. E. M. Berkhuijsen & R. Wielebinski, 279
- Schweizer, F., Miller, B. W., Whitmore, B. C., & Fall, S. M. 1996, AJ, 112, 1839
- Schaye, J. 2004, ApJ, 609, 667
- Schlegel, D. J., Finkbeiner, D. P., & Davis, M. 1998, ApJ, 500, 525
- Sengupta, C., Saikia, D. J., & Dwarakanath, K. S. 2012, MNRAS, 420, 2
- Simkin, S. M., van Gorkom, J., Hibbard, J., & Su, H.-J. 1987, *Science*, 235, 1367
- Skillman, E. D. 1987, in *Lonsdale Persson C. J., ed., Star Formation in Galaxies. NASA Conference Publication, 2466*, 263
- Skillman, E. D., & Bothun, G. D. 1986, A&A, 165, 45
- Sellwood, J. A., & Balbus, S. A. 1999, ApJ, 511, 660
- Smith, B. J. 1991, ApJ, 378, 39
- Smith, B. J. 1994, AJ, 107, 1695
- Smith, B. J. 1997, AJ, 114, 2177
- Smith, B. J., Struck, C., Kenney, J. D. P., & Jogee, S. 1999, AJ, 117, 1237
- Spitzer, L., Jr. 1990, ARA&A, 28, 71
- Stanford, S. A., & Balcells, M. 1991, ApJ, 370, 118
- Tamburro, D., Rix, H.-W., Leroy, A. K., et al. 2009, AJ, 137, 4424
- Tasker, E. J., & Bryan, G. L. 2006, ApJ, 641, 878
- Tasker, E. J., & Bryan, G. L. 2008, ApJ, 673, 810
- Thilker, D. A., Bianchi, L., Boissier, S., et al. 2005, ApJ, 619, L79
- Thornton, K., Gaudlitz, M., Janka, H.-T., & Steinmetz, M. 1998, ApJ, 500, 95
- Toomre, A. 1977, in “The Evolution of Galaxies and Stellar Populations”, eds. B. M. Tinsley

- and R. B. Larson (Yale University Press, New Haven), p. 401
- Torres-Flores, S., de Oliveira, C. M., de Mello, D. F., Scarano, S., & Urrutia-Viscarra, F. 2012, *MNRAS*, 421, 3612
- Tran, H. D., et al. 2003, *ApJ*, 585, 750
- Trancho, G., Konstantopoulos, I. S., Bastian, N., et al. 2012, *ApJ*, 748, 102
- van den Bosch, F. C. 2000, *ApJ*, 530, 177
- van der Hulst, J. M. 1979, *A&A*, 71, 131
- van der Hulst, J. M., van Albada, T. S., & Sancisi, R. 2001, *Gas and Galaxy Evolution*, 240, 451
- Verschuur, G. L., & Kellermann, K. I. 1988, *Galactic and extra-galactic radio astronomy*. Berlin: Springer, 1988, 2nd ed., edited by Verschuur, Gerrit L.; Kellermann, Kenneth I.
- Wada, K., Meurer, G., & Norman, C. A. 2002, *ApJ*, 577, 197
- Walter, F., Brinks, E., de Blok, W. J. G., et al. 2008, *AJ*, 136, 2563
- Walter, F., Martin, C. L., & Ott, J. 2006, *AJ*, 132, 2289
- Weidner, C., Bonnell, I. A., & Zinnecker, H. 2010, *ApJ*, 724, 1503
- Wevers, B. M. H. R., Appleton, P. N., Davies, R. D., & Hart, L. 1984, *A&A*, 140, 125
- Whitmore, B. C., Chandar, R., & Fall, S. M. 2007, *AJ*, 133, 1067
- Whitmore, B. C., Sparks, W. B., Lucas, R. A., Macchetto, F. D., & Biretta, J. A. 1995, *ApJ*, 454, L73
- Whitmore, B., Zhang, Q., Leitherer, C., Fall, S.M., Schweizer, F., & Miller, B. 1999, *AJ*, 118, 1551
- Wolfire, M. G., Hollenbach, D., McKee, C. F., Tielens, A. G. G. M., & Bakes, E. L. O. 1995, *ApJ*, 443, 152
- Wolfire, M. G., McKee, C. F., Hollenbach, D., & Tielens, A. G. G. M. 2003, *ApJ*, 587, 278
- Wong, T., & Blitz, L. 2002, *ApJ*, 569, 157
- Yun, M. S., Ho, P. T. P., & Lo, K. Y. 1994, *Nature*, 372, 530

## A. Notes on Individual Tails

Below we present an overview of the observed HI properties of each tail as evinced in Figure 3 and online Figure Sets 4 and 5. For more information about these systems and their SCCs, consult M11 and references therein; several dynamical and observed properties from those works are occasionally mentioned here.

### A.1. NGC 1487E

This eastern tail of a  $\approx 500$  Myr old merger remnant between similarly massed galaxies (Lee & Lee 2005), NGC 1487E contains a single SCC that is not likely real ( $f_{\text{SC}} = 0$ ). This system is the closest of the tail sample, so optical images from M11 reveal that star formation may have occurred in detectable, fainter structures. Some of these may be  $\sim 10^4 M_{\odot}$  star clusters formed *in situ*. This tail clearly favors the formation of dispersed, lower-mass structures over more massive star clusters.

Figures 4.1 and 5.1 display a high column density HI tail on  $\sim \text{kpc}$  scales, with line-of-sight velocity dispersions typically  $\sim 20 \text{ km s}^{-1}$ . The velocity field of this tail varies smoothly and produces line-of-sight velocity gradients within this tail all  $\gtrsim 5 \text{ km s}^{-1} \text{ kpc}^{-1}$ . Figure 5.1 indicates that NGC 1487E has a high fraction of turbulent and dense gas, but M11 suspected that inclination effects artificially increase the apparent HI densities measured for this system. This can easily elevate  $N_{\text{HI}}$  by a factor of 3 (0.5 dex) alone, so the actual fraction of gas above the Maybath et al. (2007) threshold (and at high mechanical energies) may be small. Consequently, the idea of a critical HI column density for massive cluster formation may still be supported in this case.

### A.2. NGC 1487W

This tail has no SCCs according to the present optical criteria. Like the eastern tail, optical detection of point sources in M11 demonstrate that this tail may preferentially exhibit a star forming morphology devoid of massive clusters. Instead, this tail hosts a large number of fainter blue ( $V - I \sim 0.0$ ) sources across the WFPC2 FOV (M11). The distributions of  $N_{\text{HI}}$ ,  $\sigma_{\text{los}}$ , and  $\Sigma_{\text{KE}}$  are very similar to those of this tail's eastern counterpart, though again it is likely that projec-

tion effects may artificially enhance the apparent column densities and affect other measured quantities. Overall,  $dv_{\text{los}}/dr_{\perp}$  in this tail appears constrained to values generally  $\lesssim 20 \text{ km s}^{-1} \text{ kpc}^{-1}$ , unlike in NGC 1487E, which shows several regions with larger velocity gradients. Otherwise,  $\sim \text{kpc}$ -scale mechanical energies across the HI debris are similar between these two tails.

### A.3. NGC 4747

The debris seen in NGC 4747 results from a  $\approx 320$  Myr old merger between its progenitor galaxy and the more massive NGC 4725 (Haynes 1979; Wevers et al. 1984). As in NGC 1487E/W, sources were observed at fainter magnitudes in M11, but few sources (6 in tail) were detected at  $M_V < -8.5$ . These also have a good probability of being real clusters based on star counts;  $f_{\text{SC}} = 0.80$  overall, while one pixel has a  $p_{\text{real}}$  value  $> 0.94$  evident in Figure 5.3.

The WSRT data used in this analysis is not as deep as the VLA/ATCA cubes for other tails, but accounting for the beam dimensions, it is still sensitive with our channel masking to  $\log N_{\text{HI}} \gtrsim 19.6 \text{ (cm}^{-2}\text{)}$ . A small amount of low column density gas is detected towards the center of the WFPC2 FOV, and has relatively low velocity dispersions ( $\lesssim 30 \text{ km s}^{-1}$ ) on its  $\approx 6 \text{ kpc}$  beam scale. We measure high velocity gradients across this HI gas ( $dv_{\text{los}}/dr_{\perp} > 30 \text{ km s}^{-1} \text{ kpc}^{-1}$ ), but the few surrounding pixels for each measurement makes this quantity prone to uncertainty. A large fraction of pixels ( $\approx 50\%$ ) are marked as unfitted for at least one of the HI properties plotted, appearing in optical images but showing no clear HI emission here. This tail appears optically prominent but relatively HI-poor.

The fact that this intermediate-stage merger has hardly any HI to the best of its cube's offered resolution is peculiar. It may be possible that it has been stripped out and/or dispersed by its recent encounter with NGC 4725. What gas remains is characterized by low kinetic energy densities ( $\sim 10^{46} \text{ erg pc}^{-2}$ ) and low column densities. However, the compliment of blue ( $V - I < 0.5$ ) point sources seen in M11 may indicate that less massive star clusters ( $\sim 10^4 M_{\odot}$ ) have formed in the past few hundreds of Myr. Thus, it appears that the formation of these structures would require a lower column density threshold than the fiducial

$\log N_{\text{HI}} \approx 20.6$  ( $\text{cm}^{-1}$ ) proposed for more massive clusters (Maybhate et al. 2007), and/or the star formation that has occurred may have helped efficiently consume/disperse an existing HI reservoir over the past few hundred Myr.

#### A.4. NGC 520

The tip of NGC 520 tail, the HI and optical condensation seen here and in M11 could be a TDG from a  $\approx 300$  Myr old interaction or a dwarf galaxy entrained in the HI tidal stream (Stanford & Balcells 1991). Within, fainter sources than the SCC magnitude cutoff were originally detected. Two sufficiently bright objects of the M11 source lists can be considered SCCs and are scattered in the HI debris, but they have low probabilities of being real clusters ( $f_{\text{SC}} = 0.06$ ).

The very center of the potential TDG contains high column density gas ( $N_{\text{HI}} \gtrsim 10^{20.6} \text{ cm}^{-1}$ ) on  $\approx 3$  kpc scales, and has a low line-of-sight velocity gradient ( $dv_{\text{los}}/dr_{\perp} < 5 \text{ km s}^{-1} \text{ kpc}^{-1}$ ). However, the  $\Sigma_{\text{KE}}$  distribution peaks barely above  $10^{46} \text{ erg pc}^{-2}$  from the moderately turbulent nature of the gas, and overall the fraction of the tail HI that is both of high column density and turbulent on  $\approx 3$  kpc scales is  $\approx 17\%$ . Once more, this environment may be somehow favorable for a smoother, diffuse star formation morphology that does not permit the formation of massive star clusters.

#### A.5. NGC 2992

NGC 2992 is  $\approx 100$  Myr into its interaction with NGC 2993 (Duc et al. 2000). It is heavily inclined along our line of sight, enhancing the tail column density by a factor of  $\approx 3$  (0.5 dex). The putative dwarf galaxy candidate at the tail tip was previously confirmed to be kinematically distinct and therefore is likely a real TDG (Brinks et al. 2004; Bournaud et al. 2004). Most of the 10 SCCs detected in this system can be found there, at least in projection. Though M11 found that across the debris, NGC 2992 is deficient in clustered star formation (to  $M_V < -8.5$ ), individually we find that about 72% of the detected sources are probably massive clusters, especially given their nonuniform distribution.

The  $N_{\text{HI}}$  measurements for in-tail pixels are all high in projection, with almost 80% of the gas

having apparent ( $\approx 4$  kpc-scale) column densities  $\log N_{\text{HI}} \gtrsim 20.6$  ( $\text{cm}^{-2}$ ). This is also evident in the  $\Sigma_{M_{\text{HI}}}$  map, where regions with mass densities  $\gtrsim 10 M_{\odot} \text{ pc}^{-2}$  are apparent, despite the saturation of HI known to occur around that (deprojected) density. We detect a reasonably uniform  $\sigma_{\text{los}}$  distribution, with values ranging from  $\approx 20$ – $80 \text{ km s}^{-1}$ , while our map of  $dv_{\text{los}}/dr_{\perp}$  highlights a region with a locally shallow ( $< 5 \text{ km s}^{-1} \text{ kpc}^{-1}$ ) velocity gradient within the TDG and its SCCs.

In terms of the SCCs, K–S tests reveal that the distributions of tail pixels with and without at least one SCC are similar for all properties except  $N_{\text{HI}}$ , owing to the cluster candidates situated in the high column density TDG (though note the small sample size for the former category). Again, though it is not clear from Figure 5.5, these SCCs appear superimposed over a region of especially shallow large-scale velocity gradient in Figure 4.5. And even if the  $N_{\text{HI}}$  values were decreased by 0.5 dex to roughly account for tail geometry and orientation, Figure 5.5 would show that these SCCs would still be embedded in HI gas with higher column densities than the Maybhate et al. (2007) threshold.

#### A.6. NGC 2993

The interacting, similarly massed counterpart to NGC 2992, NGC 2993 presents a relatively face-on orientation. High  $N_{\text{HI}}$  areas on  $\approx 4$  kpc scales also register high moment-measured velocity dispersions ( $\sigma_{\text{los}} \gtrsim 40 \text{ km s}^{-1}$ ) and kinetic energy densities ( $\log \Sigma_{\text{KE}} \gtrsim 47 \text{ erg pc}^{-2}$ ), and there appears to be a strong dependence of  $\sigma_{\text{los}}$  on  $N_{\text{HI}}$  in Figure 5.6. About 70% of these sources should be clusters, but only half lie in areas of high  $N_{\text{HI}}$ . Most are still found in regions of high kinetic energy density ( $\log \Sigma_{\text{KE}} \gtrsim 46 \text{ erg pc}^{-2}$ ). However, K–S tests show that the distributions of SCC-empty and SCC-laden pixels are not independent for any measured quantity.

#### A.7. NGC 2782E

A  $\approx 200$  Myr-old minor merger, NGC 2782 exhibits an eastern tail that may be the distorted remnant of the smaller galaxy (Smith 1994). Interestingly, the optical tail extends beyond the HI tail. Approximately 57% of the  $\approx 4$  kpc-scale tail pixels exhibit HI of supercritical column densities

and turbulent velocity dispersions. Many pixels are unfitted ( $f_{\text{unfit}} \approx 0.24$ ), so the fraction of high-column density, turbulent gas relative to the total HI reservoir is higher.

The velocity field of the HI debris varies smoothly across the eastern side of the debris ( $dv_{\text{los}}/dr_{\perp} \lesssim 5 \text{ km s}^{-1} \text{ kpc}^{-1}$ ), and changes more sharply on the western side ( $dv_{\text{los}}/dr_{\perp} \gtrsim 10 \text{ km s}^{-1} \text{ kpc}^{-1}$ ). Velocity dispersions can also range from  $\sim 10 \text{ km s}^{-1}$  on the eastern side to  $\gtrsim 60 \text{ km s}^{-1}$  in the west. The  $\Sigma_{\text{KE}}$  map follows this trend accordingly. We compute a high  $f_{\text{SC}}$  value (0.96) for the 56 SCCs in this tail; thus most should be clusters. These nearly all populate the turbulent-high  $N_{\text{HI}}$  region of Figure 5.7. They also lie in pixels with  $\log \Sigma_{\text{KE}} > 46.5 \text{ erg pc}^{-2}$ , and span a range of  $dv_{\text{los}}/dr_{\perp}$  measurements (between  $0\text{--}30 \text{ km s}^{-1} \text{ kpc}^{-1}$ ).

The pixels with SCCs also comprise different distributions of  $N_{\text{HI}}$ ,  $\sigma_{\text{los}}$ ,  $\Sigma_{\text{KE}}$ ,  $dv_{\text{los}}/dr_{\perp}$ , and  $\Sigma_{\text{KE}}$ , with K-S tests producing results  $< 5 \times 10^{-4}$  in all cases. Cluster formation may occur in regions of preferentially higher column density, higher line-of-sight velocity dispersions, high kinetic energy densities, and a broad range of  $\sim 10$  kpc-scale velocity gradients in this tail. These gradients may be too broadly constructed (measuring differences over areas larger than the radio beam) to accurately trace the kinematic structure of local SCC-conducive environments, however, particularly where the velocity field varies rapidly towards the central galaxy.

#### A.8. NGC 2782W

If NGC 2782E is the consumed minor galaxy of the NGC 2782 interacting pair, this western tail may be the HI-rich tidal debris of the primary galaxy. While Smith et al. (1999) detect CO emission in the eastern tail, none is found in NGC 2782W by Braine et al. (2001). Perhaps correspondingly, far fewer SCCs (6) are detected in this tail. However, as mentioned in Section 4.1, the work of Torres-Flores et al. (2012) and our star counts imply that  $\approx 52\%$  of these sources should be star clusters. In particular, Torres-Flores et al. (2012) find these sources are  $\approx 10^4 M_{\odot}$ ,  $\approx$  a few Myr old clusters. This is consistent with H $\alpha$  observations of Knierman et al. (2012) and their conclusion that ongoing star formation does occur in this tail, but at low effi-

ciency compared to other extragalactic environments. For no properties do the distributions of SCC-carrying and SCC-devoid pixels appear statistically distinct.

The central debris shows large regions with very shallow velocity gradients ( $dv_{\text{los}}/dr_{\perp} \lesssim 5 \text{ km s}^{-1} \text{ kpc}^{-1}$ ), and generally a less extensive range of line-of-sight velocity dispersions ( $\sigma_{\text{los}} \approx 10\text{--}30 \text{ km s}^{-1}$ ) on  $\approx 4 \text{ kpc}$  scales. Compared to NGC 2782E, This tail has qualitatively similar gas fractions in the turbulent-high  $N_{\text{HI}}$  quadrant of Figure 5.8. The western tail has a lower fraction of unfitted pixels, however, ( $f_{\text{unfit}} \approx 0.1$ ), and a higher percentage of gas with relatively low values of  $dv_{\text{los}}/dr_{\perp}$ . The distributions of  $N_{\text{HI}}$ ,  $\sigma_{\text{los}}$ , and  $\Sigma_{\text{KE}}$  also peak at broadly lower values for NGC 2782W than for the eastern debris.

#### A.9. NGC 2444

A young ( $\approx 100 \text{ Myr}$  old) tail, the debris of NGC 2444 formed quickly from a possible high-speed encounter (Appleton et al. 1987; c.f. Koopmann et al. 2008). Gas profiles indicate the HI is kinematically disturbed ( $\sigma_{\text{los}} \approx 20\text{--}80 \text{ km s}^{-1}$  for most of the pixels) on  $\approx 8 \text{ kpc}$  scales. There are no pixels with  $N_{\text{HI}}$  above the fiducial threshold, and the  $dv_{\text{los}}/dr_{\perp}$  map of Figure 4.9 shows the velocity gradients across the tail are mostly below  $\approx 10 \text{ km s}^{-1} \text{ kpc}^{-1}$ .

5 of the SCCs detected lie within the tidal debris;  $\approx 3$  of them may be star clusters based on star counts ( $f_{\text{SC}} = 0.63$ ). Moreover, the pixels upon which they appear superimposed do not seem to have different distributions of  $N_{\text{HI}}$ ,  $\sigma_{\text{los}}$ ,  $dv_{\text{los}}/dr_{\perp}$ , or  $\Sigma_{\text{KE}}$  than do all tail pixels (to the extent to small sample of SCC-containing pixels allows). Most ( $\approx 95\%$ ) of the  $\sim 8 \text{ kpc}$ -scale HI has kinetic energy densities above  $10^{46} \text{ erg pc}^{-2}$  and has a relatively shallow velocity gradient, but does not have a widespread cluster population. If there are indeed a few clusters in the SCC source list for this system, either they did not need kpc-scale high column density HI gas to form, our resolution is too poor to see more local concentrations of HI, or previous star formation dispersed the gas efficiently in the past 100 Myr. Given the optical faintness of this tail (it does not register on WFPC2 images), it may be unlikely star formation feedback has played much of a role in this case.



### A.10. NGC 2535

The approximately face-on NGC 2535 debris results from a young ( $\approx 100$  Myr) interaction with NGC 2536 (Hancock et al. 2007). Measurements of  $\approx 6$  kpc-scale velocity dispersions for these profiles ranges from  $10\text{--}50$  km s $^{-1}$ , typically, with the regions of highest  $\sigma_{\text{los}}$  and lowest  $dv_{\text{los}}/dr_{\perp}$  ( $\lesssim 4$  km s $^{-1}$  kpc $^{-1}$ ) closely mirroring the most optically prominent regions seen in M11. Most of the 36 in-tail SCCs also fall in these regions,  $\approx 93\%$  of which should be star clusters. From K–S tests, the pixels that contain them appear to have generally higher values of  $N_{\text{HI}}$ , and lower values of  $dv_{\text{los}}/dr_{\perp}$ , but do not arise from different distributions of  $\sigma_{\text{los}}$  and  $\Sigma_{\text{KE}}$  compared to all tail pixels. Several pixels have multiple SCCs “within,” so their  $p_{\text{real}}$  values are higher ( $>0.94$ ); these occupy the regions of turbulent, high  $N_{\text{HI}}$ , low  $dv_{\text{los}}/dr_{\perp}$ , and high  $\Sigma_{\text{KE}}$  in Figure 5.10.

### A.11. NGC 6872E

NGC 6872 is  $\approx 150$  Myr into an interaction with the smaller companion galaxy IC 4970 (Horellou & Koribalski 2003; Horellou & Koribalski 2007). NGC 6872E is the easternmost FOV of the enormous eastern tail, featuring a moderate percentage of high column density HI (about 50% of the gas has  $\log N_{\text{HI}} > 20.6$  cm $^{-2}$  on  $\approx 16$  kpc scales). The line-of-sight velocity dispersion ranges from  $\approx 20$  km s $^{-1}$  from the tail edges to  $\approx 100$  km s $^{-1}$  in the interior.

The central region of the debris is also host to an extensive population of SCCs (over a hundred are detected here), which is also coincident with areas of shallow large-scale velocity gradients ( $dv_{\text{los}}/dr_{\perp} \lesssim 5$  km s $^{-1}$  kpc $^{-1}$ ). For all considered properties except  $dv_{\text{los}}/dr_{\perp}$ , the pixels hosting SCCs comprise different distributions than those of tail pixels that do not; their distributions tend to peak at higher values of  $N_{\text{HI}}$ ,  $\sigma_{\text{los}}$ , and therefore also  $\Sigma_{\text{KE}}$ . According to Table 3, about 94% of these sources should be clusters, and pixels with multiple SCCs have even higher probabilities of containing at least one. As seen in Figure 5.11, of these pixels of highest cluster-containing probability, almost all have kinetic energy densities  $>10^{47}$  erg pc $^{-2}$ , and column densities  $>10^{20.6}$  cm $^{-2}$ . The positions of the SCCs are also aligned with regions

of H $\alpha$  emission (Bastian et al. 2005; Mihos et al. 1993).

There are still cluster candidates in pixels with “subcritical”  $N_{\text{HI}}$ , however—including roughly 6–10% of them that lie in regions unfitted by several HI properties—and many of these may be real. It is then again a question of whether this  $N_{\text{HI}}$  threshold is important, these clusters had formed in previously high column density HI in the past 150 Myr that has since dispersed or been consumed, or instrumental effects prevent an assessment of HI properties at crucially lower (pc–kpc) scales. A non-negligible fraction of the tail pixels are unfitted ( $f_{\text{unfit}} \approx 0.15$ ), so these effects are certainly possible. For NGC 6872, the physical scale may be especially important, as the cube for this system has a particularly large beam, both in angular and physical extent.

### A.12. NGC 6872W

This western debris highlights the base of the eastern tail of the NGC 6872 system, displaying a central clump of moderate HI emission around the Maybhate et al. (2007) limit, immersed in a tail of lower column density gas ( $\approx 80\%$  of the in-tail pixels) that follows the optical structure seen in M11. Flanking the HI tail is bright optical debris that both contains SCCs and is devoid of detectable neutral hydrogen. This helps account for the large fractions of unfitted SCC-hosting and SCC-empty pixels ( $\approx 0.4$  and  $0.3$ , respectively). The densest regions exhibit velocity dispersions up to  $\approx 100$  km s $^{-1}$ . Here the velocity structure is not of a smoothly rotating, extended disk, but has a number of kinematically distinct components, as elaborated in the modeling of Horellou & Koribalski (2007). Thus, the  $dv_{\text{los}}/dr_{\perp}$  map, showing measurements of line-of-sight velocity gradients across pixels separated by more than one beam, displays areas with seemingly steep gradients. Internally, however, the local gradients may be shallower.

In either case, the 101 SCCs detected appear as widely distributed as the kinematically varied HI debris. K–S tests demonstrate that the pixels that contain them are generally not different in terms of  $N_{\text{HI}}$ ,  $\sigma_{\text{los}}$ , or  $\Sigma_{\text{KE}}$ , and while their distribution of  $dv_{\text{los}}/dr_{\perp}$  values appears statistically distinct, the aforementioned spatial resolution of these NGC 6872 data make this difficult to interpret. 18 of these sources exist in exclusively op-

tically defined debris, and the remaining sources mostly in low- $N_{\text{HI}}$  areas are also likely to be actual clusters ( $f_{\text{SC}} = 0.93$ ). Even the pixels with the highest probabilities of having at least one cluster generally have  $N_{\text{HI}}$  values below the fiducial cutoff, while their high  $\sigma_{\text{los}}$  measurements ensure that their mechanical energy densities remain all above  $\log \Sigma_{\text{KE}} = 46 \text{ erg pc}^{-2}$ .

### A.13. NGC 1614N

The northern region of the NGC 1614 tidal debris is HI-poor ( $f_{\text{unfit}} \approx 0.89$ ), with concrete detections only at the very northern and southern edges of the central host galaxy. It is conversely prominent in the optical, with galactic material arranged in warped rings around the merger remnant of an interaction thought to have begun  $\approx 750$  Myr ago (Neff et al. 1990 and references therein). The few pixels with detectable HI emission show high  $\sigma_{\text{los}}$  ( $\approx 75 \text{ km s}^{-1}$ ). These isolated clumps of neutral hydrogen have high column densities on  $\approx 5 \text{ kpc}$  scales, and appear to have larger-scale velocity gradients  $dv_{\text{los}}/dr_{\perp} \sim 10 \text{ km s}^{-1} \text{ kpc}^{-1}$ , though the paucity of HI pixels makes this comparative measurement admittedly uncertain.

19 SCCs are found interspersed in the optical debris, with only 3 lodged in the HI debris (several occupy the same pixels). Thus, K–S tests cannot be performed on the different pixel distributions. But the majority of the SCCs should be clusters ( $f_{\text{SC}} = 0.95$ ), so clusters are detected in this tail regardless of HI content. NGC 1614N results from a very late-stage interaction, so these sources may also be several hundred Myr old and had initially formed while surrounded by an HI medium that has since dispersed, been ionized, or consumed. While the photometry of M11 cannot age-date the SCCs, their red  $V - I$  colors ( $V - I \sim 1$ ) may imply these clusters are older (or reddened by extinction).

NGC 1614 is luminous at infrared wavelengths and contains a powerful nuclear starburst (Alonso-Herrero et al. 2001). It is possible that the HI in the northern tail has been eliminated by central winds, photoionized by the central starburst, or photoionized by past star formation. Hibbard et al. (2000) contends that a mean R-band surface brightness of  $\approx 23 \text{ mag arcsec}^{-2}$ —depending on the HI column density and dimensions of the tidal debris—is required for the stellar

population to effectively rid itself of the warm neutral medium on these scales. NGC 1614N is one of the few debris fields in the M11 sample to exceed this surface brightness (its F606W-band surface brightness is  $\approx 22 \text{ mag arcsec}^{-2}$ , which in terms of photometric bandpasses is close to  $R$ ), so it is possible mass *in situ* photoionization of the tidal HI has occurred in the past.

### A.14. NGC 1614S

The HI of the southern tail of NGC 1614 is confined to a “stub” extending from the southernmost tip of the merger remnant; most tail pixels are optically defined ( $f_{\text{unfit}} \approx 0.89$ ). Its HI characteristics are similar to those of the northern debris; the measurable HI here is of comparably high column density ( $\log N_{\text{HI}} \gtrsim 20.6 \text{ cm}^{-2}$ ) and with line-of-sight velocity dispersions ranging from the instrumental limit to  $\approx 75 \text{ km s}^{-1}$ . The ranges of velocity gradients are also similar, with  $dv_{\text{los}}/dr_{\perp} \approx 5\text{--}15 \text{ km s}^{-1} \text{ kpc}^{-1}$ .

The main difference is the number and distribution of SCCs. 30 sources are located in the combined optical and HI tail, with most of them falling in the HI stub. Once more, a high fraction of them are probable star clusters ( $f_{\text{SC}} = 0.96$ , with  $p_{\text{SC}}$  exceeding this number for many pixels that contain more than one SCC). The sources here are very blue ( $V - I \lesssim 0$ ; M11), indicating star formation might be relatively recent and/or ongoing. These sources trace out the high- $N_{\text{HI}}$ , high- $\Sigma_{\text{KE}}$ , and turbulent regions of the HI parameter space of Figure 5.14, and the pixels that have them do not appear different with respect to those properties than HI pixels overall.

It is however curious that the positions of these SCCs is offset by a few arcseconds from the regions of highest column density as seen in the  $N_{\text{HI}}$  map of Figure 4.14. The HI may be in the process of being locally consumed or swept out by current star formation. Approximately 42% of the equally high probability SCCs are found in optically bright yet HI-unfitted regions, so these sources may be further examples of past feedback and HI dispersal or consumption sometime over the course of this tail’s  $\approx 750$  Myr lifetime. Unfortunately,  $VI$  observations of M11 do not permit accurate age-dating of cluster candidates to provide evidence for this age-dependent HI removal. If generous K–S probability cutoff is employed, the distributions of

$dv_{\text{los}}/dr_{\perp}$  between pixels and without SCCs appear marginally independent. But again the low spatial resolution for this especially distant object may confuse this quantification of the large-scale velocity field.

#### A.15. NGC 4038A/B/C

This well-studied merger has two large, symmetric tails of ages  $\approx 450$  Myr (K03 and references therein). WFPC2 images of the ABC positions along these tails reveal them to be optically faint, diffuse, and all but devoid of SCCs (K03; M11). As a whole they are poor in HI, with very little gas at or above the Maybath et al. (2007) threshold on  $\approx \text{kpc}$  scales. Across the WFPC2 pointings, it appears  $\approx 30$ – $80\%$  of the tail pixels are classified as unfitted by at least one HI characteristic. This gas is relatively kinematically unperturbed, with  $\sigma_{\text{los}} \lesssim 25 \text{ km s}^{-1}$ , and much of the gas showing dispersions less than the turbulent-thermal cutoff. Consequently, less than  $\approx 5$ – $20\%$  of the gas has kinetic energy densities  $> 10^{46} \text{ erg pc}^{-2}$ .

3 SCCs are found in NGC 4038A, and 1 is found in the NGC 4038B and NGC 4038C FOVs each. They all have low values for  $f_{\text{SC}}$  and their host pixels have correspondingly low values of  $p_{\text{real}}$  (0–0.24); thus they are likely point source contaminants. They populate too few pixels to conduct K–S tests between distributions of HI characteristics. Unlike the active, luminous interior and bridge regions of the merger, the tails of this system are extraordinarily quiescent in terms of ongoing star formation.

#### A.16. NGC 3256E/W

Dynamically, the tails of NGC 3256 are about 400 Myr old (K03), resulting from an ongoing major merger of two similarly massed galaxies. The channel width of the NGC 3256 data cube is wide ( $\approx 33.5 \text{ km s}^{-1}$ ), so each pixel has few channels of signal. Combined with the beam size and sensitivity of the data, uncertainties in HI properties are high for pixels with  $N_{\text{HI}} \lesssim 10^{20} \text{ cm}^{-2}$ . The vertical “tail” of constant  $\sigma_{\text{los}}$  in Figures 5.18 and 5.19 represents the instrumental limit in determining velocity dispersions. Much of the HI gas in these tails is of high column density and line-of-sight velocity dispersions on scales of  $\approx 5 \text{ kpc}$ ; we find  $\approx 72\%$  and  $88\%$  of tail pixels has those proper-

ties in the eastern and western tails, respectively. The distribution of  $dv_{\text{los}}/dr_{\perp}$  values in both tails is very broad, ranging from 0– $50 \text{ km s}^{-1} \text{ kpc}^{-1}$ , while the distribution of that property is skewed towards lower values for NGC 3256W.

The western tail has fewer pixels with at least one unfitted HI characteristic (by a factor of  $\approx 4$ – $10$ ). 32 SCCs are located in the eastern tail, and 51 are in the west. Given the calculated values for  $f_{\text{SC}}$  (0.50–0.60), a little over a dozen sources in the east and about 30 sources in the west may be genuine star clusters. This strong level of contamination results from this system’s low galactic latitude ( $b \approx 11^\circ$ ), and led K03 to conclude that the eastern tail did not have a statistically significant widespread cluster population, and the western tail did. This is still true; the eastern tail may have only a handful of real clusters, but they are spread throughout the  $\approx 1720 \text{ kpc}^2$  tail area and do not constitute a significant population.

Most of the SCCs in either tail populate the high  $N_{\text{HI}}$  and high  $\sigma_{\text{los}}$  parameter space of the neutral medium. According to K–S tests, pixels containing SSCs in the eastern tail may have typically higher line-of-sight velocity dispersions, but do not comprise unique distributions compared to all pixels in terms of other measured properties. Conversely, the pixels hosting cluster candidates in NGC 3256W might have generally shallower velocity gradients with a generous interpretation of that K–S result. The central “spine” of the western debris is a region of low  $dv_{\text{los}}/dr_{\perp}$  ( $\lesssim 5 \text{ km s}^{-1} \text{ kpc}^{-1}$ ), an attribute absent in the eastern tail. Perhaps a combination of this and the higher fraction of high column density gas contributes to the factor of  $\sim 3$  increase of possible clusters in the western tail over the east.

#### A.17. NGC 7252E/W

NGC 7252 is a late-stage ( $\approx 730$  Myr old; K03) merger between two comparably massed galaxies. The channel width of this system’s data cube is the widest of the debris sample ( $\approx 42.5 \text{ km s}^{-1}$ ). The HI in both debris fields is relegated to the tips of the straight and narrow eastern and western tails, and is characterized by low column and mass densities on  $\approx 1.5 \text{ kpc}$  scales and steep velocity gradients ( $dv_{\text{los}}/dr_{\perp} \gtrsim 15 \text{ km s}^{-1} \text{ kpc}^{-1}$ ) on larger scales. The latter may be attributed in part to the velocities ascribed to the low-signal edge

pixels, which can be uncertain. The moderately turbulent kinematics of the gas helps to offset the low mass densities and maintains the kinetic energy densities of much of the HI above  $10^{46}$  erg  $\text{pc}^{-2}$ .

Comparable numbers of SCCs are in either tail (11 and 17 for east and west, respectively), with fairly comparable values of  $f_{\text{SC}}$  (0.80 and 0.89). In 7252E these sources are widely distributed, many of which are situated in the HI-poor optical debris ( $f_{\text{unfit}}^{\text{SCC}} \approx 0.40$ ). Two neighboring sources are located in a clump of diffuse optical emission, which is slightly offset from the central high- $N_{\text{HI}}$  region seen in Figure 4.20. Pixels that contain the SCCs in this tail do not seem to arise from dissimilar distributions of  $N_{\text{HI}}$ ,  $\sigma_{\text{los}}$ ,  $\Sigma_{\text{KE}}$ , or  $dv_{\text{los}}/dr_{\perp}$  than all HI tail pixels.

The same is true for the western tail, except for the velocity dispersion, for which SCC-laden pixels seem to have a more narrow range of values ( $\sigma_{\text{los}} \approx 10\text{--}30$  km  $\text{s}^{-1}$ ). 11 sources are dispersed throughout the primarily optically defined tidal tail, with  $\approx 40\%$  in especially HI-poor regions (in comparison,  $f_{\text{unfit}} \approx 0.30$ ). A few HI pixels in the only high mass density region at the end of the tail contain 6 of them. This region of the debris has the lowest  $dv_{\text{los}}/dr_{\perp}$ , and is the only part of Figure 5.21 that shows  $N_{\text{HI}} > 10^{20.6}$   $\text{cm}^{-2}$ . These sources belong to the prominent optical/HI-defined TDG in the western tail (Hibbard et al. 1994). The fact that this one region of obvious clustered star formation is the only region of high column density HI and contains a large number of SCCs (the superimposed black points in Figure 5.21) indicates that, at least in this case, the Maybhate et al. (2007)  $N_{\text{HI}}$  threshold may be important in forming star clusters. These few HI pixels do not stand out in the distribution of  $\Sigma_{\text{KE}}$ ; a combination of high mechanical energy densities and column densities may be observationally important in finding SCCs in situations like this.

### A.18. NGC 3921S

NGC 3921 is the most distant interaction of the sample (84.5 Mpc), and accordingly its HI cube has the worst spatial resolution of the debris surveyed here ( $\approx 2$  kpc for each pixel; roughly 4 times that for the size of the beam). The optical completeness limit for this tail as analyzed by K03 is also the worst of the sample, with a  $V$ -band 50%

completeness limit at  $M_V = -8.8$ . Therefore, it is probable that some SCCs are missing from the source list.

Its HI debris has velocity dispersions on this scale of  $\approx 5\text{--}30$  km  $\text{s}^{-1}$ , and has a smoothly varying velocity structure with shallow larger-scale velocity gradients ( $dv_{\text{los}}/dr_{\perp} \lesssim 5$  km  $\text{s}^{-1}$  kpc $^{-1}$ ). Approximately 10% of the tail pixels has a high column density, and is confined to the long tail-shaped structure that extends from the north to the south of the  $N_{\text{HI}}$  map. Of the 14 SCCs in the HI or optical debris, only two are embedded in this relatively higher- $N_{\text{HI}}$  material, and most are dispersed throughout the debris. About 87% of these sources should be clusters, and one pixel that contains two sources—part of a short chain of sources that extends from the north of the optical image—correspondingly has a high chance of containing at least one massive cluster.

These SCC-supporting pixels do not appear to have statistically unique distributions of measured HI quantities compared to all HI pixels, and all but one of them lie in regions of low column density ( $\log N_{\text{HI}} < 20.6$   $\text{cm}^{-2}$ ). Their moderate velocity dispersions mean that their kinetic energies are still greater than the fiducial  $10^{46}$  erg  $\text{pc}^{-2}$ . As is the case with other tails, the low spatial resolution, feedback from star formation (certainly possible over the  $\approx 460$  Myr lifetime of the tail; K03), and/or a revised  $N_{\text{HI}}$  threshold might at least partially explain the detection of these handful of reasonably probable clusters. The particularly poor resolution makes it especially possible that sub-kpc clumps of denser HI gas are being effectively diluted by the size of the beam for this system, especially when they are found in closer, better resolved tails.